

# Protostellar Outflows: Identification, Parameter Estimation and Simulation

## Project Report

Sanjana Gupta

Affiliation: Ashoka University

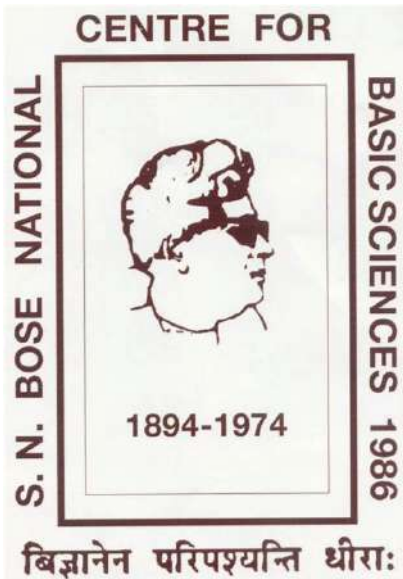
Supervisor: Dr. Tapas Baug

Affiliation: S.N. Bose National Centre for Basic Sciences

Start Date: 3rd July 2024

Submission Date: 16th August 2024

INSPIRE IVR No.: 202100010807



# Contents

<b>1</b>	<b>Project Completion Certificate</b>	<b>iii</b>
<b>2</b>	<b>Acknowledgement</b>	<b>iv</b>
<b>3</b>	<b>Objectives</b>	<b>1</b>
<b>4</b>	<b>Introduction of Research Topic</b>	<b>1</b>
<b>5</b>	<b>Theoretical Framework of Topic</b>	<b>2</b>
5.1	Star formation . . . . .	2
5.1.1	Star formation mechanism by disk accretion . . . . .	2
5.2	Outflows in disk accretion process . . . . .	3
5.3	Identification of Outflows . . . . .	4
<b>6</b>	<b>Profile of Organization/Research Lab</b>	<b>5</b>
<b>7</b>	<b>Methodology Followed</b>	<b>5</b>
7.1	Data used for identification of outflows . . . . .	5
7.1.1	ALMA . . . . .	6
7.1.2	HII regions analysed . . . . .	6
7.1.3	Procedure . . . . .	6
<b>8</b>	<b>Analysis and Interpretation of Research Project</b>	<b>7</b>
8.1	Identification of Outflows . . . . .	7
8.1.1	Moment Maps . . . . .	7
8.1.2	Intensity vs. Velocity Plots . . . . .	13
8.1.3	Position-Velocity Diagrams . . . . .	17
8.2	Estimation of Outflow Parameters . . . . .	29
8.2.1	Core Identification . . . . .	29
8.2.2	Temperature . . . . .	30
8.2.3	Dynamical Properties of Outflows . . . . .	31
8.3	Modelling Protostellar Outflows . . . . .	36
8.3.1	PLUTO Code . . . . .	36
8.3.2	Results with different parameter setup . . . . .	39
<b>9</b>	<b>Conclusion &amp; Suggestion of Research Project</b>	<b>51</b>
<b>10</b>	<b>Future Scope</b>	<b>52</b>
<b>11</b>	<b>Results Achieved</b>	<b>52</b>

<b>12 References</b>	<b>53</b>
<b>13 Declaration</b>	<b>54</b>

# 1 Project Completion Certificate

1. IVR Number or Application Ref. No.: 202100010807
2. Name of INSPIRE Scholar: SANJANA GUPTA
3. Name of College where Scholar is studying: ASHOKA UNIVERSITY
4. Name of University to which above College is affiliated: ASHOKA UNIVERSITY
5. Bank Account Number of Scholar: 35588440272
6. IFSC Code: SBIN0003692
7. Mobile No. and Email Address of Scholar: 9433581344, sanjana.gupta207@gmail.com
8. Title of Project: Protostellar Outflows: Identification, Parameter Estimation and Simulation
9. Broad Subject Area of Research Project: Astrophysics
10. Project Duration (in weeks): 7
11. Date of Start of Research Project: 03/07/2024
12. Date of Completion of Research Project: 16/08/2024
13. Supervisor Name: Dr. Tapas Baug
14. Designation of Supervisor: Associate Professor
15. Affiliation of Supervisor:
  - (a) Department: Astrophysics and High Energy Physics
  - (b) College: -
  - (c) University: S. N. Bose National Centre for Basic Sciences
  - (d) Address: Salt Lake Bypass Road, Near Calcutta Heart Clinic & Hospital, Sector 3, Salt Lake City, Kolkata, West Bengal 700106
  - (e) Mobile no. and Email Address: 99744 07543, tapasbaug@bose.res.in
16. Major Specialization area of Supervisor: Observational Astronomy

*Tapas Baug.*

(Seal & Signature of Supervisor)

**Dr. Tapas Baug**  
Assistant Professor  
Department of Astrophysics and High Energy Physics  
S.N. Bose National Centre for Basic Sciences  
Kolkata - 700106, India

Date: 18.10.2024

## 2 Acknowledgement

I would like to express my sincere gratitude to Dr. Tapas Baug for his invaluable guidance and support throughout this project. His patient explanation of the theory of protostellar outflows and detailed explanations of observational techniques were instrumental in my understanding and successful completion of this work. Writing the code would not have been possible without his clear and thorough explanations of the underlying logic and techniques. I am especially grateful for the daily meetings, during which he helped me debug the code and collaboratively address any issues with the data. Dr. Baug's mentorship has made this my most rewarding internship experience to date.

### 3 Objectives

1. Advance understanding of outflows in the star formation process, focusing on the observational characteristics of protostellar outflows.
2. Determine physical parameters of outflow lobes within massive protoclusters associated with ultracompact HII regions.
3. Utilize high-resolution observations from the Atacama Large Millimeter Array (ALMA) to analyze CO (3–2), HCO<sup>+</sup> (4–3), and HCO<sup>+</sup> (1–0) emission line data, tracing components of the shocked environment and dense gas surrounding young stellar objects.
4. Extract key physical parameters such as outflow mass, momentum, energy, and mass-loss rates through analytical methods.
5. Conduct numerical simulations using the PLUTO code to model jet propagation and replicate observed characteristics of protostellar outflows, investigating the impact of varying parameters on outflow morphology and kinematics.

### 4 Introduction of Research Topic

Outflows are a prevalent feature in many accreting astrophysical systems, especially those characterized by rotation and magnetic fields. These outflows, often observed as bipolar streams or collimated jets, are found across a wide range of phenomena, including young stellar objects (YSOs), symbiotic stars, protoplanetary and planetary nebulae, supernovae, accreting neutron stars, microquasars, and active galactic nuclei [1]. The presence of outflows in these systems is nearly universal and plays a significant role in their dynamic behavior.

In the realm of star formation, protostellar outflows are particularly important. They are detectable across various parts of the electromagnetic spectrum—from radio waves to X-rays—using both continuum and spectral line observations. These techniques provide valuable information about the physical conditions, chemical compositions, radial velocities, and motions within the outflows [2]. Advances in wide-field visual and near-infrared (IR) imaging, mid-IR observations from space, and high-resolution interferometric techniques in the centimeter and millimeter wavelengths have greatly enhanced our ability to study these outflows in detail.

The nature of protostellar outflows is diverse, ranging from highly focused jets to broad, wide-angle winds, and in some cases, nearly isotropic and explosive patterns [3]. Variations in their morphology and velocity fields reveal differences in ejection velocity, mass-loss rates, flow orientation, and degrees of collimation, highlighting the complex interactions between the outflows and their surrounding environments [4].

The strength of these outflows generally increases with the luminosity of the source but diminishes as the system evolves. Younger outflows, typically traced by molecules like CO, SiO, H<sub>2</sub>O, and

H<sub>2</sub>, are relatively small, while older outflows, often extending to parsec scales, are better traced by shock-excited atoms and ions such as hydrogen recombination lines, [SII], and [OII]. These outflows are not only crucial for driving the dynamics of the systems they originate from but also inject momentum and energy into their surroundings, playing a key role in regulating star formation [5].

The velocities of these outflows can vary widely, from a few kilometers per second in young stars to nearly the speed of light in systems driven by neutron stars and black holes [6]. Within a 1-kiloparsec radius of the Sun, hundreds of YSO outflows have been identified. Detailed spectral line observations enable precise measurements of radial velocities and the determination of physical parameters such as density, temperature, and pressure under a broad range of conditions [7].

## 5 Theoretical Framework of Topic

### 5.1 Star formation

Two prominent models for massive star formation are: (i) core accretion through a disk and (ii) competitive accretion [8]. This project will focus on disk accretion and the outflows generated by this process.

#### 5.1.1 Star formation mechanism by disk accretion

Star formation primarily takes place within dense, cold regions of molecular gas, commonly known as molecular clouds [2]. The overall efficiency of this process is generally low, with only a small fraction of the mass within nearby molecular cloud complexes converting into stars [8]. Nevertheless, there are specific localized areas within these clouds where the efficiency of star formation is significantly higher, often leading to the formation of bound star clusters [4].

The process of star and planet formation begins with the collapse of a molecular core. In these molecular clouds, star formation initiates in the densest regions, referred to as cores [1]. These cores serve as the nurseries of star formation, where the gas density is sufficient to overcome thermal pressure, triggering gravitational collapse. Initially, the mass is concentrated within the core, but it is gradually processed through an accretion disk—funneling inwards onto the protostar and outwards through an outflow [2].

As the core collapses, conservation of angular momentum naturally leads to the formation of a rotating disk surrounding the emerging protostar [4]. This disk, composed of gas and dust, is essential for channeling material onto the developing star, while simultaneously dispersing the remaining mass from the core [6].

Circumstellar disks are an inevitable consequence of angular momentum conservation during the gravitational collapse that leads to star formation. During the initial collapse phase, as more distant material with higher angular momentum falls inward, a disk quickly forms [8]. This disk then extends out to the centrifugal radius, which grows rapidly over time, according to the relation  $R(t) \propto \Omega^2 t^3$ , where  $\Omega$  is the angular rotation rate of the core. The disk evolves rapidly, with its final

size and mass being highly sensitive to the infall time and the properties of the core [3]. Initially, these disks rapidly funnel material onto the protostar, but as the surrounding molecular core is depleted or dispersed, the accretion rate diminishes, leaving a residual amount of material in the disk [9].

Following the initial collapse phase, the process transitions into an extended period of disk accretion. During this phase, angular momentum within the disk is gradually redistributed, with a small fraction of particles at the disk's outer regions gaining most of the angular momentum [5]. This redistribution allows the majority of the disk's mass to accrete onto the central protostar [7]. As the protostar accumulates mass, the disk evolves, and under favorable conditions—such as the right temperature, composition, and angular momentum distribution—some of the remaining disk material may coalesce to form planets [8].

Disk accretion is not only the most prevalent but also the most extensively studied mechanism of star formation, particularly for stars of low to intermediate mass. This process is closely linked to the formation of planetary systems, which typically emerge from the remnants of the disk following the primary accretion phase [3]. The formation of planets is contingent upon the conditions within the disk being optimal, with various factors needing to align for planet formation to occur [6].

Circumstellar disks also play a crucial role in regulating star formation through the ejection of gas in the form of jet-like outflows. These outflows are vital for managing the angular momentum within the disk, thereby facilitating the continued growth of the central star [4]. The long-term evolution of the star-disk system is largely governed by the rate at which angular momentum is transported within the disk, influencing both the accretion process and the potential for planet formation, and ultimately shaping the final structure and dynamics of the system [7].

## 5.2 Outflows in disk accretion process

Protostellar outflows, driven by magnetic fields, are an intrinsic feature of accretion onto protostars. These outflows manifest as high-velocity jets that are a natural consequence of angular momentum conservation during the accretion process. In the early stages of star formation, a portion of the material accreted from the surrounding envelope or disc is expelled. This material is ejected as collimated jets that sweep up surrounding gas, forming molecular outflows. These outflows are often more detectable than the accretion discs themselves, particularly in star-forming regions [see 1, for more details].

The dynamics of protostellar outflows are closely linked to inflow processes. Magnetic stresses within the circumstellar disc-protostar system are believed to be responsible for launching the outflowing material [10]. In early stages of massive star formation, outflows are often well-collimated, but as stars evolve, the outflows can become less collimated. This transition is partly due to increased turbulence and the impact of an expanding H II region, which changes the physical conditions at the base of the outflow. Young massive stars, which are still accreting and generating strong molecular outflows, often display these well-collimated outflows, whereas older sources with detectable UC HII regions and main-sequence stars exhibit less collimated flows [11].

For low-mass stars, the formation of bipolar outflows driven by the accretion disc is well-established both theoretically and observationally [9]. These outflows are fundamental in the star formation process, providing crucial kinetic energy to the surrounding material. They reduce the accretion rate onto the protostar, impact the temperature of the clump and disc, and enhance fragmentation within the filaments. This process helps regulate star formation by injecting mechanical energy into the parent molecular cloud, contributing to the cloud's turbulence and stabilizing it against gravitational collapse [12].

Several models have been proposed to explain the formation and characteristics of protostellar outflows:

1. **Wind-Driven Shell Models:** These models propose that a wide-angle radial wind from the protostar blows into the surrounding ambient material, creating a thin swept-up shell. This model is particularly effective in explaining older outflows with large lateral extents and low collimation [4].
2. **Turbulent Jet Models:** In this scenario, Kelvin-Helmholtz instabilities at the boundary between the jet and the surrounding environment lead to the formation of a turbulent mixing layer. This turbulence entrains the surrounding molecular gas, creating a more chaotic outflow. Increased turbulence that might be driven by high accretion disk-to-stellar mass ratios, increased radiation pressure, and high plasma temperatures can lead to a breakdown in the ideal MHD conditions and result in less collimated outflows [13].
3. **Jet-Driven Bow Shock Models:** Here, a highly collimated jet propagates through the surrounding material, producing a pair of shocks (jet and bow shocks) at its head. This interaction creates an outflow shell around the jet, with episodic variations in the mass-loss rate resulting in a chain of knots and shocks along the jet axis [6].
4. **Circulation Models:** These models suggest that molecular outflows are formed not by jets or winds but by infalling matter that is deflected by high MHD pressure in a quadrupolar circulation pattern around the protostar. Local heating then accelerates the outflow above escape speeds [9].

### 5.3 Identification of Outflows

Disks around young stars display a temperature gradient, with higher temperatures closer to the star and cooler temperatures further out. This gradient results in the disk emitting radiation across a broad spectrum, from infrared to millimeter wavelengths, which can be observed using infrared and radio telescopes. By correlating specific wavelengths with radial distances within the disk, detailed models of the disk's structure can be developed, even from photometric data that does not resolve the disk.

The Infrared Astronomical Satellite (IRAS) played a crucial role in advancing infrared observations, enabling the first large-scale statistical studies of protoplanetary disks. Subsequently, sensitive

millimeter-wavelength detectors uncovered that many of these disks contain enough material to potentially form planetary systems akin to our own. Interferometry at millimeter wavelengths allowed for the resolution of these disks, confirming their flattened and rotating nature. The development of interferometric techniques at longer baselines and shorter wavelengths, including the submillimeter range with instruments such as the Submillimeter Array (SMA) and the Atacama Large Millimeter Array (ALMA), has significantly enhanced our understanding of disk structure and evolution. For this project, ALMA data has been employed to further investigate disk characteristics.

## 6 Profile of Organization/Research Lab

The S. N. Bose National Centre for Basic Sciences operates as an independent research institute that was founded in 1986. It is supported by the Department of Science and Technology of the Government of India and is officially recognized as a registered society. The Centre was created to honor Professor S. N. Bose, a prominent figure in the realm of theoretical physics, celebrated for his significant contributions to Quantum Mechanics and Quantum Statistics.

At this Centre, the Department of Astrophysics and High Energy Physics undertakes a wide variety of research initiatives that encompass theoretical studies, observational projects, and experimental work in modern astrophysics and cosmology. The department focuses on critical areas of investigation, such as the processes involved in the formation of massive stars, the characteristics of exoplanets, the physics governing brown dwarfs, and the behavior of black holes located in remote galaxies.

Furthermore, the department delves into topics like neutrino physics and stellar evolution, as well as the dynamics of cataclysmic variables. It also conducts research on the formation of complex molecules across different astrophysical contexts. A significant aspect of the department's mission is to promote advancements in astronomical instrumentation, which helps ensure that it remains at the cutting edge of scientific exploration and innovation in the field.

## 7 Methodology Followed

### 7.1 Data used for identification of outflows

The molecular clouds were observed between May 18 and 20, 2018 (UTC) as part of ALMA Cycle 5, under the project code 2017.1.00545.S (PI: Tie Liu). These observations utilized 43 12-meter antennas in the C43-1 configuration. To capture multiple molecular lines, four spectral windows in Band 7 were employed, centered at 343.2, 345.1, 354.4, and 356.7 GHz. These frequencies are effective tracers of infalling and outflowing gas, as well as the continuum. The observational data was sourced from Baug et al. (2020) [3].

## 7.1 ALMA

The Atacama Large Millimeter Array (ALMA) is a cutting-edge astronomical interferometer located in the Atacama Desert of northern Chile. Comprised of 66 highly precise radio antennas, ALMA is designed to observe electromagnetic radiation at millimeter and submillimeter wavelengths, specifically within the range of 0.32 to 3.6 mm. Situated at an altitude of 5,000 meters (16,000 feet) on the Chajnantor plateau, near the Llano de Chajnantor Observatory and the Atacama Pathfinder Experiment, ALMA's array consists of 50 main antennas, each with a 12-meter diameter, functioning together as a single radio interferometer. The antennas can be arranged in various configurations, with separations ranging from 150 meters to 16 kilometers, giving ALMA a powerful variable "zoom" feature. This capability allows it to produce images with exceptional clarity, often surpassing those of the Hubble Space Telescope. In ALMA's smallest 12m array configuration, it can achieve a resolution ranging from 0.5" at a wavelength of 0.5 mm (650 GHz) to 8.5" at a wavelength of 7.5 mm (40 GHz).

### 7.1 HII regions analysed

Source	RA (J2000)	Dec (J2000)	$V_{LSR}$ (km/s)	Distance (kpc)
IRAS 14498-5856 CO [3-2]	14 53 42	-59 08 56	-50.03	$3.2 \pm 0.5$
IRAS 14498-5856 HCO <sup>+</sup> [1-0]	14 53 42	-59 08 56	-50.03	$3.2 \pm 0.5$
IRAS 14498-5856 HCO <sup>+</sup> [4-3]	14 53 42	-59 08 56	-50.03	$3.2 \pm 0.5$
IRAS 16060-5146 CO [3-2]	16 09 52	-51 54 54	89.95	$5.2 \pm 0.6$
IRAS 16060-5146 HCO <sup>+</sup> [1-0]	16 09 52	-51 54 54	-89.95	$5.2 \pm 0.6$
IRAS 16060-5146 HCO <sup>+</sup> [4-3]	16 09 52	-51 54 54	-89.95	$5.2 \pm 0.6$
IRAS 16272-4837 CO [3-2]	16 30 59	-48 43 53	-46.42	$3.2 \pm 0.3$

Table 1: Sources Analysed

### 7.1 Procedure

The 3D FITS cubes were first examined using SAOImageDS9, beginning with the high-end redshifted and blueshifted velocities, as these channels are minimally affected by emission from the central clouds. This approach facilitated the identification of both bipolar and single outflows associated with continuum sources. Various techniques were employed to detect these outflows, and all analysis and parameter calculations were conducted using custom Python scripts. The 3D data cubes, representing position-position-velocity information, were read and manipulated using packages such as `SpectralCube` and `Astropy`. For the data cubes where the spectral axis is in frequency, it is converted to velocity using code, and that data cube is then used for further analysis.

Initially, the data cubes were imported using Astropy, followed by the generation of moment maps as detailed in the Moment Maps section. Subsequently, intensity profiles were plotted as a function of velocity to analyze the spectral characteristics of the observed region. Utilizing the

python-based `Dendrogram` algorithm the star-forming core was identified, and a region file was created to delineate its boundaries accurately.

An intensity versus velocity plot specific to the core was produced to verify the local standard of rest velocity ( $V_{\text{LSR}}$ ), which is assumed to represent the systemic velocity of the core. This verification is crucial as subsequent parameter calculations are conducted with the core serving as the reference frame. In the original Intensity vs. Velocity plot, a velocity window centered around  $V_{\text{LSR}}$  was selected to isolate the core emission. The regions of the plot to the right and left of this window correspond to blue-shifted (gas moving toward the observer) and red-shifted (gas moving away from the observer) components, respectively.

Masks corresponding to the blue-shifted and red-shifted regions were created to segregate these components effectively. Separate moment maps were then generated for each of these masked regions to identify and analyze the outflows emanating from the core. Following the identification process, the moment map FITS files for both blue-shifted and red-shifted emissions were individually examined in SAOImageDS9, where the trajectories of the outflows were meticulously traced and marked.

To further comprehend the kinematic structures of these outflows, Position-Velocity (PV) diagrams were constructed along the marked paths. These PV diagrams facilitate a detailed analysis of the velocity distribution along the outflow paths and serve as a verification tool to confirm the presence and authenticity of the identified outflow regions.

## 8 Analysis and Interpretation of Research Project

### 8.1 Identification of Outflows

#### 8.1 Moment Maps

In spectral analysis, moments provide a mathematical framework to extract various properties from the spectral data, where the spectral axis can represent velocity, frequency, wavelength, or energy. These moments are calculated using the intensity  $I_v$ , which is the flux or measured intensity in a given spectral channel.

The **zeroth moment** ( $M_0$ ) represents the integrated intensity over the entire spectral line, essentially summing up the total emission across all spectral channels. It is given by the integral:

$$M_0 = \int I_v dv$$

This moment reflects the total amount of emission in the data cube, with units dependent on both the intensity and the spectral axis (e.g., Jy/beam \* km/s).

The **first moment** ( $M_1$ ) corresponds to the intensity-weighted mean velocity of the spectral line, providing a measure of the central velocity around which most of the emission is concentrated. It is calculated as:

$$M_1 = \frac{\int v I_v dv}{\int I_v dv} = \frac{\int v I_v dv}{M_0}$$

This moment is critical for understanding the average motion of the emitting material, with units matching those of the spectral axis (e.g., km/s).

The **higher-order moments**, starting from the second moment ( $M_2$ ), offer insights into the distribution and spread of the spectral line. Specifically, the second moment represents the velocity dispersion or the width of the spectral line, indicating how spread out the velocities are around the mean:

$$M_N = \frac{\int I_v (v - M_1)^N dv}{M_0}$$

For  $N = 2$ , this gives the velocity dispersion, with units that are the square of the spectral axis units (e.g., km<sup>2</sup>/s<sup>2</sup>). This moment is crucial for analyzing the turbulent motions or thermal broadening within the observed region [14].

A code is written that generates and visualizes moment maps from a `SpectralCube` object, utilizing Python packages such as `astropy`, `matplotlib`, and `numpy`. The code extracts three key moment maps: integrated intensity (Moment 0), intensity-weighted velocity (Moment 1), and velocity dispersion (Moment 2). To facilitate plotting, the RA (Right Ascension) and DEC (Declination) pixel coordinates are converted into degrees. This conversion is performed by the `get_pixel_locations` function, which retrieves the necessary reference pixel, reference coordinate, and coordinate increment from the FITS header. The corresponding degree coordinates are then calculated by applying the increment to each pixel and adding the reference coordinate. The use of `astropy.units` ensures proper handling of the unit conversions, yielding RA and DEC values in degrees.

For visualization, `matplotlib` is employed to create a figure comprising three subplots, each representing one of the moment maps. Color maps and normalization are applied using the `simple_norm` function from `astropy.visualization`. The normalization employs a square root stretch and is adjusted to capture 85% of the data range, which effectively enhances the contrast and highlights the most relevant features within the maps. The moment maps are displayed using the `imshow()` function, with clearly labeled axes, color bars, and appropriate tick parameters. An annotation of the source name is added to the Moment 0 plot for reference. After generating the plots, the code constructs a directory path using the `os` package, creates the directory if it does not already exist, and saves the figure as a PDF file.

Moment maps are first created from the original data cube, and then they are created for the blueshifted and redshifted regions separately to clearly identify the outflows.

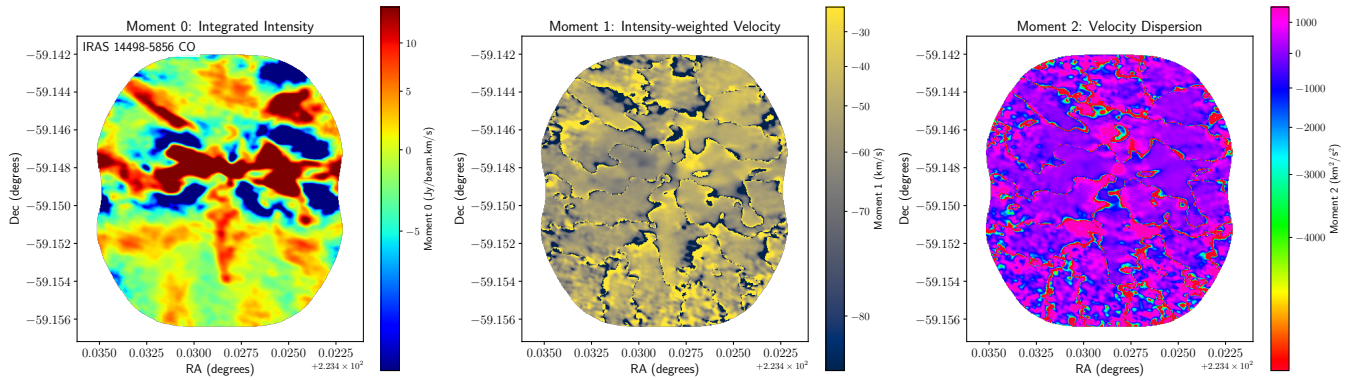


Figure 1: Moment Maps for the source IRAS 14498-5856 CO

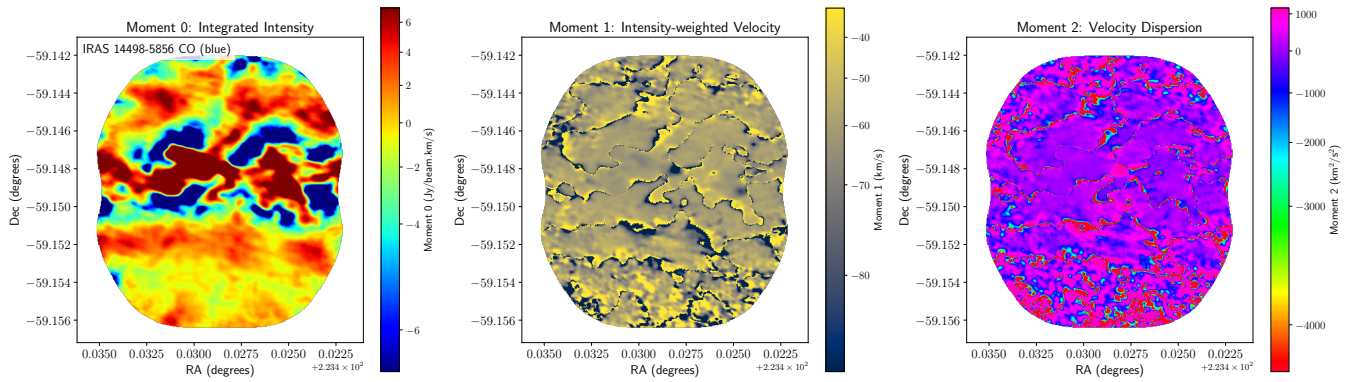


Figure 2: Moment Maps for the blue-shifted part of the source IRAS 14498-5856 CO

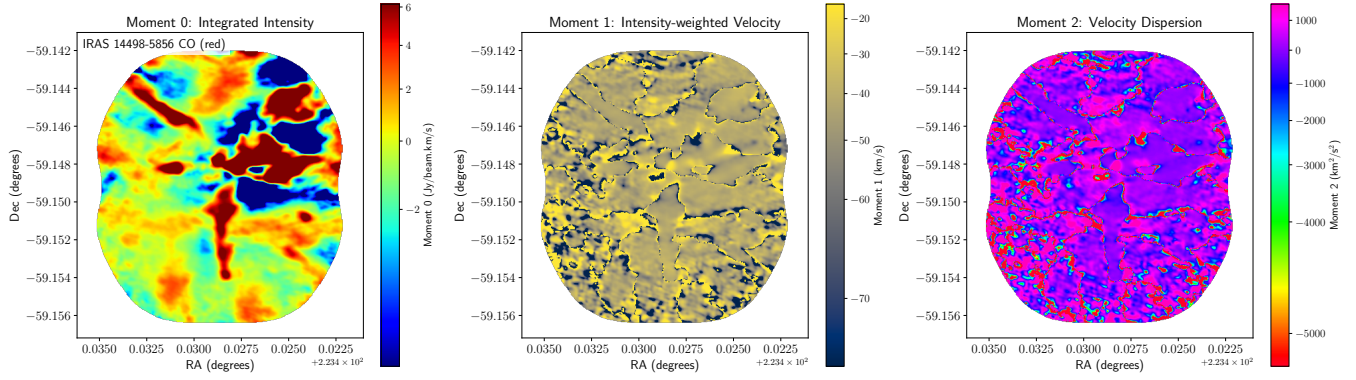
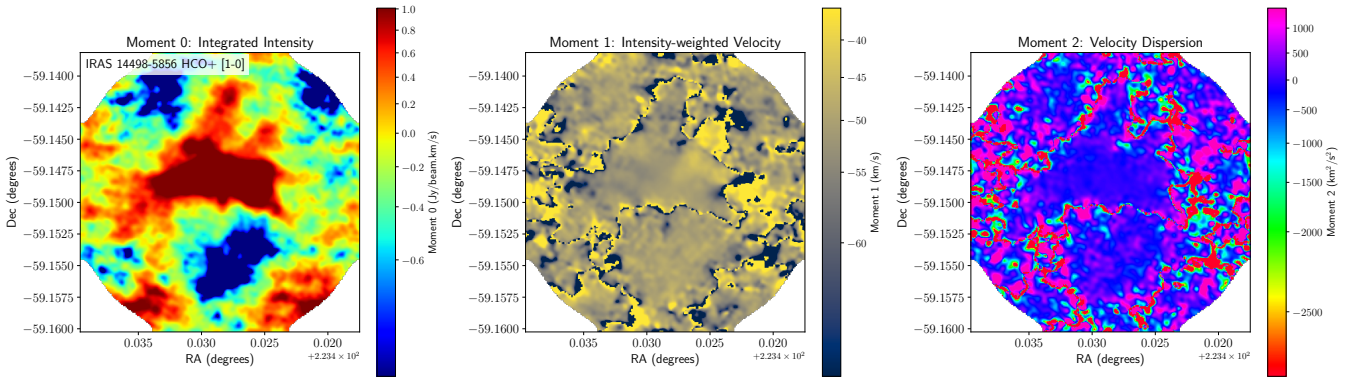
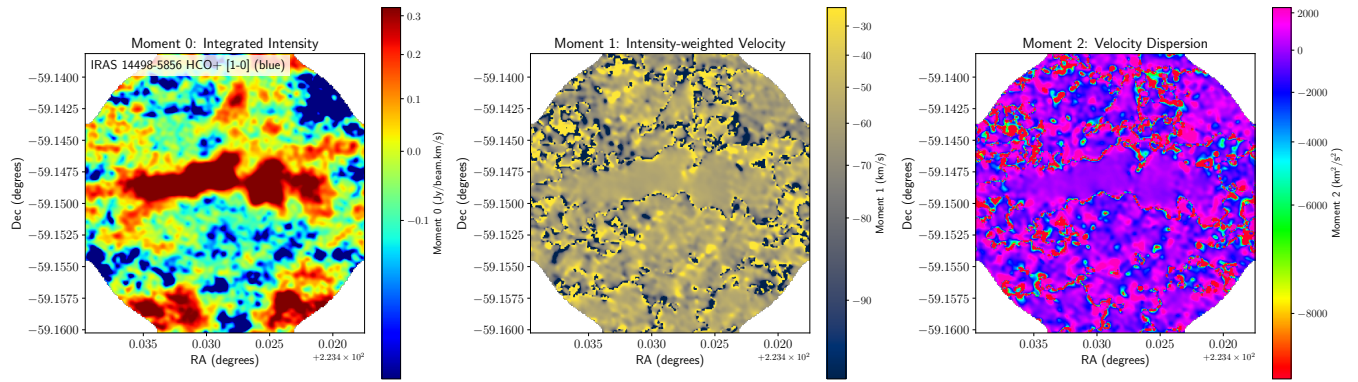
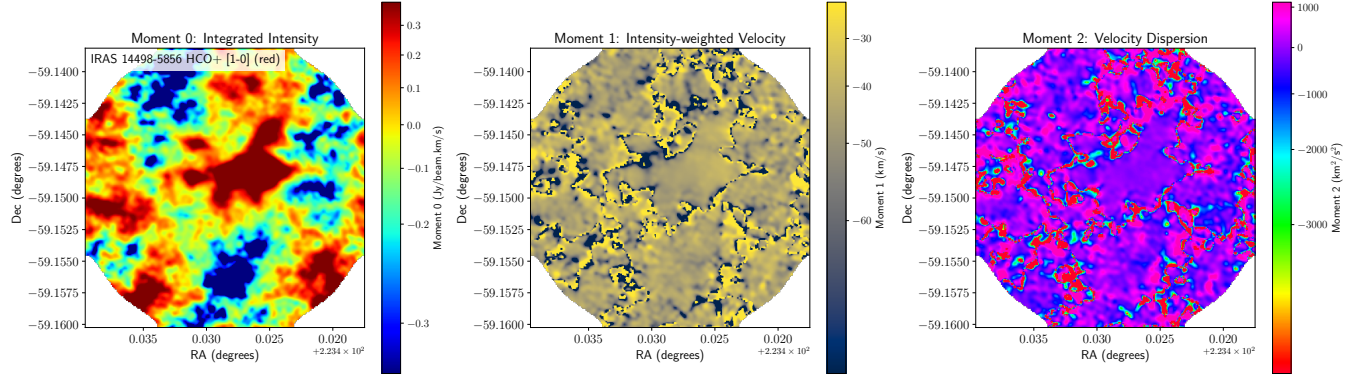


Figure 3: Moment Maps for the red-shifted part of the source IRAS 14498-5856 CO

Figure 4: Moment Maps for the source IRAS 14498-5856 HCO<sup>+</sup> [1-0]Figure 5: Moment Maps for the blue-shifted part of the source IRAS 14498-5856 HCO<sup>+</sup> [1-0]Figure 6: Moment Maps for the red-shifted part of the source IRAS 14498-5856 HCO<sup>+</sup> [1-0]

The horizontally oriented bipolar outflow is evident in both the CO and HCO<sup>+</sup> datasets. In addition to the prominent bipolar outflow, several other outflows are detected in the CO data. However, these additional outflows exhibit lower intensities, which likely accounts for their absence in the HCO<sup>+</sup> data due to its comparatively lower resolution. The relative faintness of these outflows is further corroborated by the CO Moment 0 map (Figure 1), where the intensity associated with the bipolar outflow is significantly higher than that of the other three outflows.

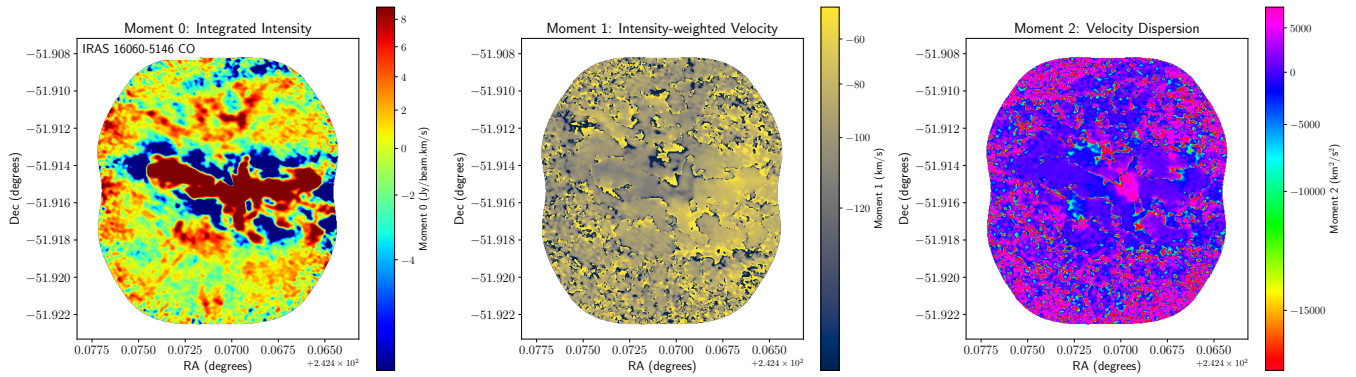


Figure 7: Moment Maps for the source IRAS 16060-5146 CO

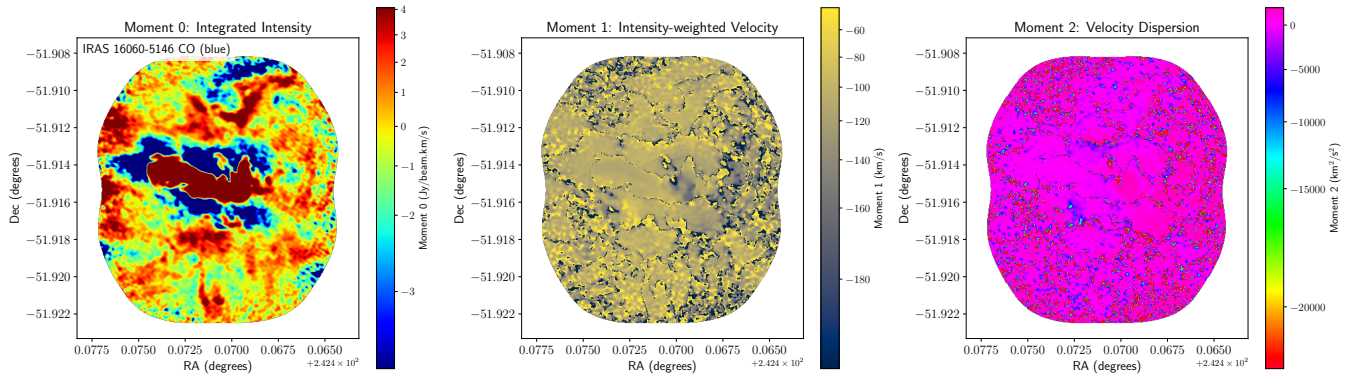


Figure 8: Moment Maps for the blue-shifted part of the source IRAS 16060-5146 CO

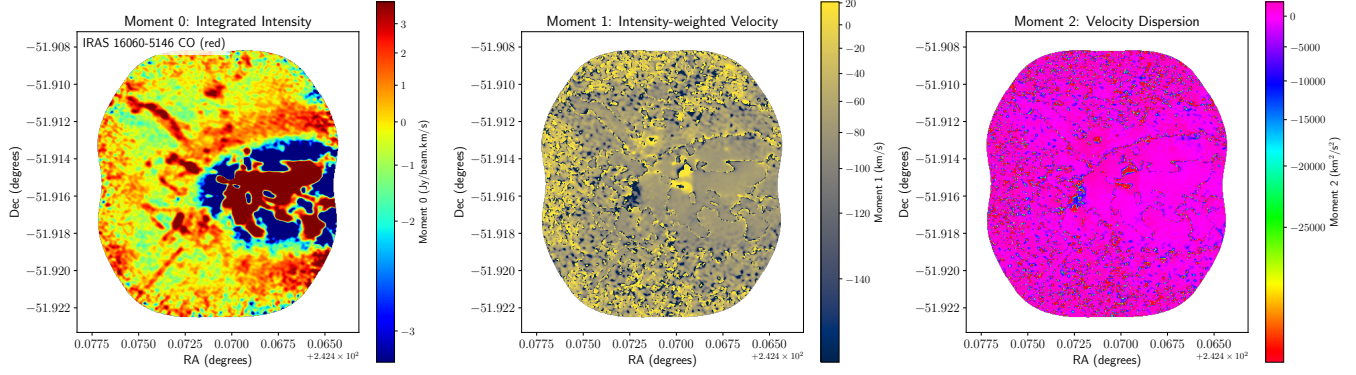


Figure 9: Moment Maps for the red-shifted part of the source IRAS 16060-5146 CO

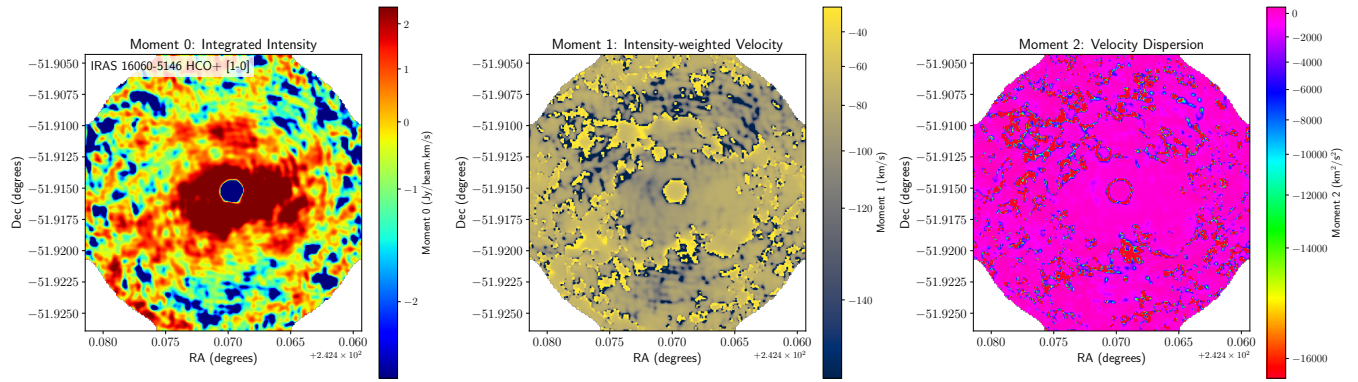


Figure 10: Moment Maps for the source IRAS 16060-5146 HCO<sup>+</sup> (1-0)

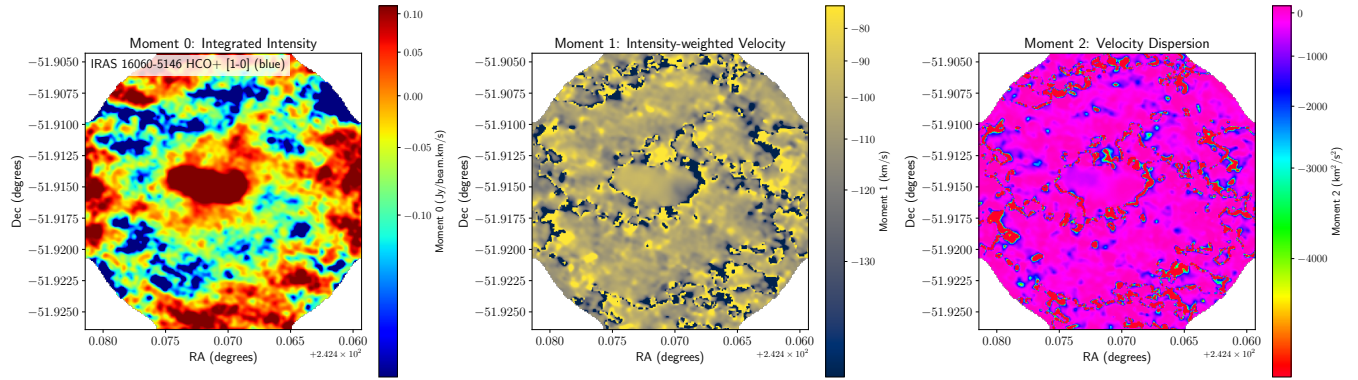


Figure 11: Moment Maps for the blue-shifted part of the source IRAS 16060-5146 HCO<sup>+</sup> (1-0)

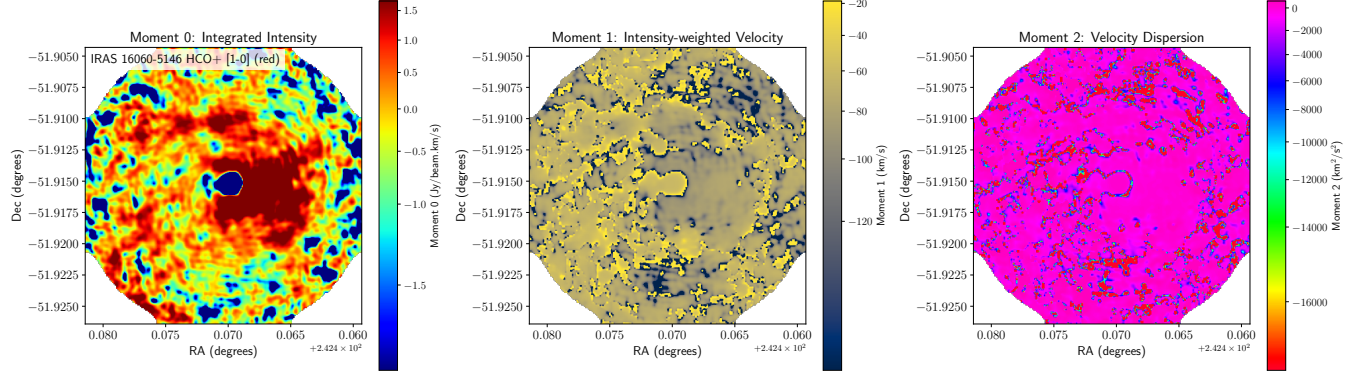


Figure 12: Moment Maps for the red-shifted part of the source IRAS 16060-5146 HCO<sup>+</sup> (1-0)

In this source, a prominent bipolar outflow is the primary feature observed, detectable in both the CO and HCO<sup>+</sup> datasets. It is noteworthy that in the HCO<sup>+</sup> data, the intensity of the core region appears to have been excessively subtracted during the calibration process, particularly in the handling of the continuum data. This over-subtraction may affect the accuracy of the intensity measurements in the core region, potentially leading to an underestimation of the emission from this area.

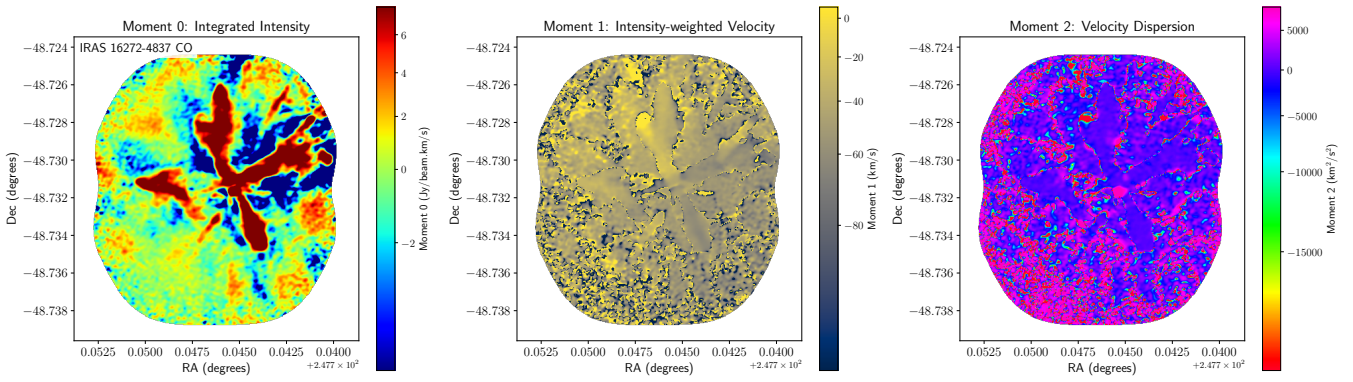


Figure 13: Moment Maps for the source IRAS 16272-4837 CO

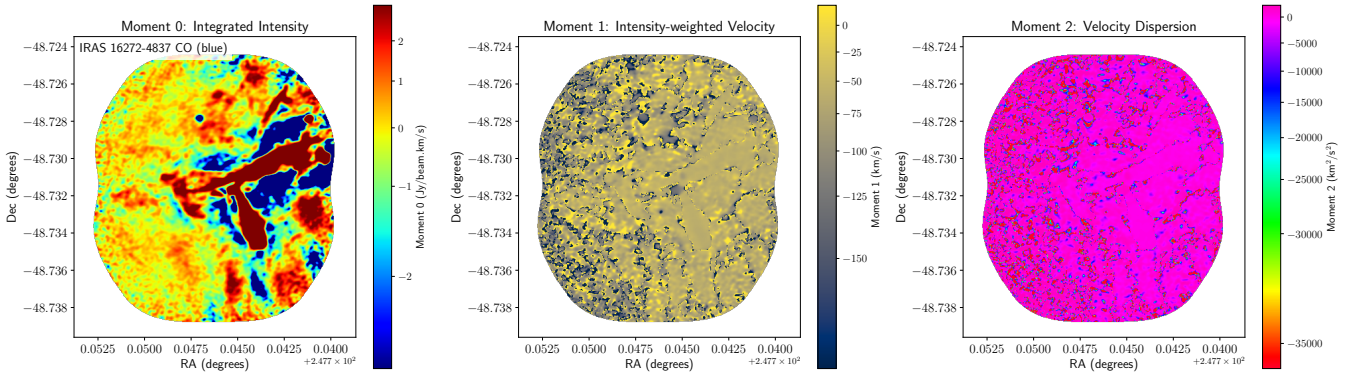


Figure 14: Moment Maps for the blue-shifted part of the source IRAS 16272-4837 CO

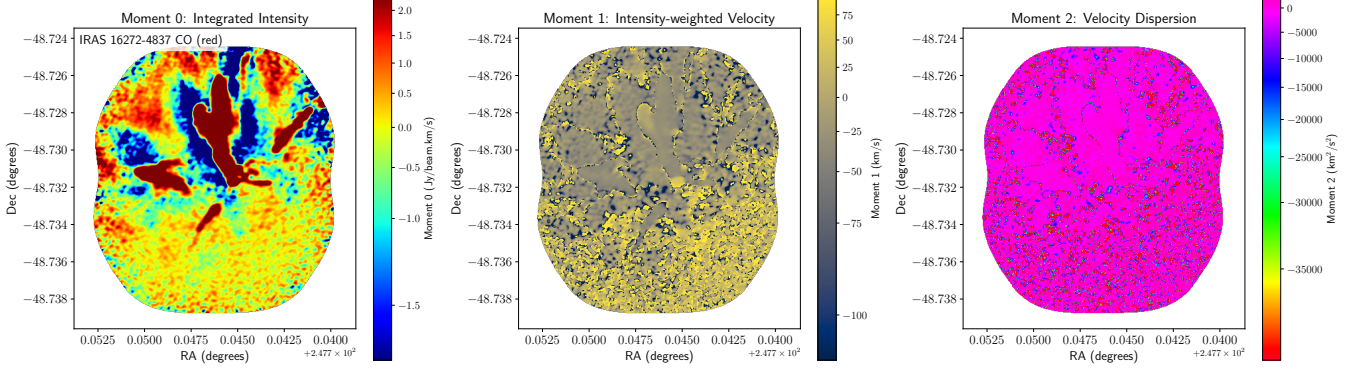


Figure 15: Moment Maps for the red-shifted part of the source IRAS 16272-4837 CO

## 8.1 Intensity vs. Velocity Plots

A function `process_spectral_cube` is designed to handle and analyze spectral data cubes, which contain intensity information across various velocities. The function's behavior depends on whether the input data pertains to CO or HCO<sup>+</sup> molecules, and it follows distinct procedures based on this distinction.

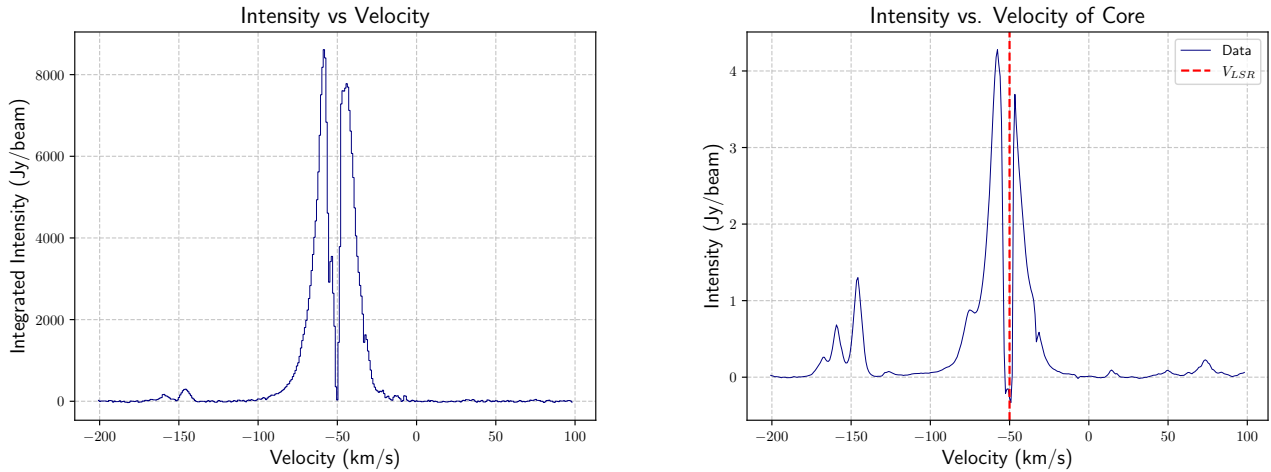
Initially, the function reads the spectral data from a FITS file using `fits.open` and extracts both the data and the header. For HCO<sup>+</sup> data, it retrieves parameters from the header related to the spectral axis, including the reference value, pixel scale, and reference pixel. These parameters are used to convert the spectral axis from pixels to velocity units (km/s). The header is updated to reflect this velocity scale, and the data is saved to a new FITS file with these updated parameters using `fits.PrimaryHDU` and `writeto`.

In contrast, when processing CO data, the function additionally uses the rest frequency from the header to calculate the velocity scale. This involves converting the frequency values to velocity values using the rest frequency, which adjusts the spectral axis accordingly. This updated information is also saved to a new FITS file.

Following the preparation of the spectral data, the function calculates the intensity versus velocity profile by summing the intensity values across the spatial dimensions of the data cube. This sum provides a profile showing how the total intensity varies with velocity. The function then generates a plot of this profile, with the velocity on the x-axis and the integrated intensity on the y-axis.

The function further analyzes the core region of the spectral data. It extracts this region based on a predefined spatial boundary provided through a region file using functions such as `parse_ds9_reg_file` and `calculate_bounds`. Within this region, it calculates the average intensity profile. For HCO<sup>+</sup> data, a Gaussian function is fitted to this profile using `curve_fit` to determine parameters such as the central velocity and width of the emission line. These parameters are used to define bounds for filtering velocity ranges. In the case of CO data, fixed bounds around the local standard of rest (LSR) velocity are employed. This approach is based on the expectation that the line emission from the core region should follow a Gaussian profile due to Doppler broadening, with a sharp absorption line at the LSR velocity. This method is applied to HCO<sup>+</sup> data but not to CO data, as the latter also includes emissions from the cloud, making it extremely difficult to fit Gaussian profiles to the data.

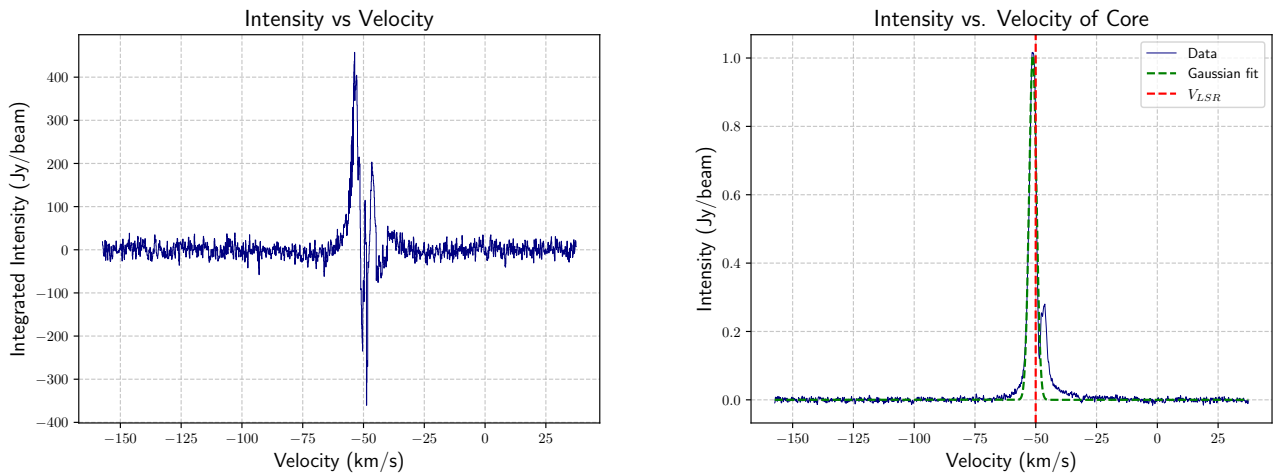
Finally, the function creates masks to isolate regions of low and high velocities based on the previously determined bounds. These masks are applied to the data cube to produce two separate data cubes: one for blue-shifted (low-velocity) regions and another for red-shifted (high-velocity) regions. These filtered cubes are saved as separate FITS files using `fits.PrimaryHDU` and `writeto`. The data cubes are then used to plot the individual moment maps of the blue-shifted and red-shifted regions.



(a) Intensity vs. Velocity plot for the HII region containing the source IRAS 14498-5856 CO

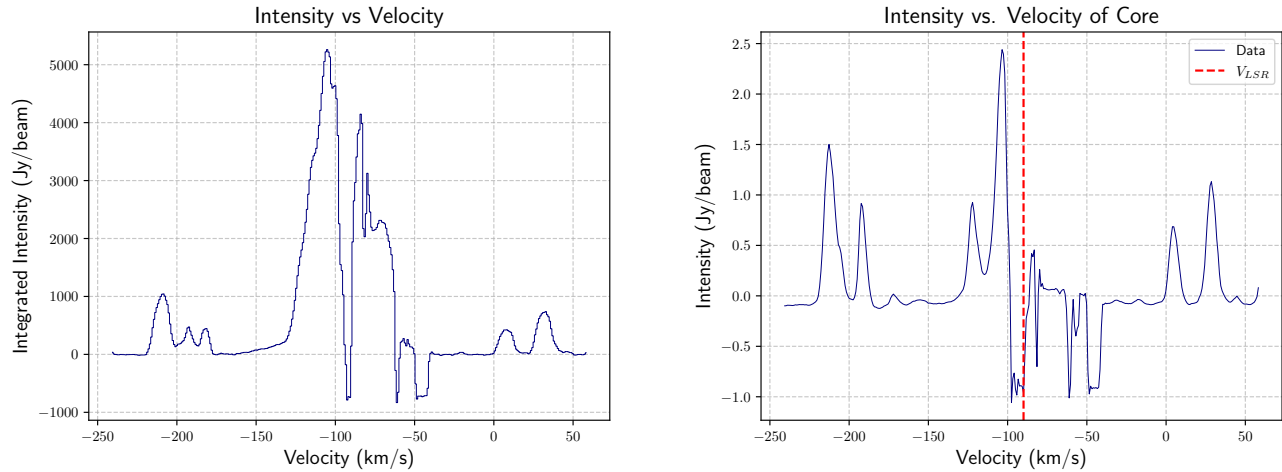
(b) Intensity vs. Velocity plot for the major star forming core in the HII region

Figure 16

(a) Intensity vs. Velocity plot for the HII region containing the source IRAS 14498-5856 HCO<sup>+</sup>

(b) Intensity vs. Velocity plot for the major star forming core in the HII region

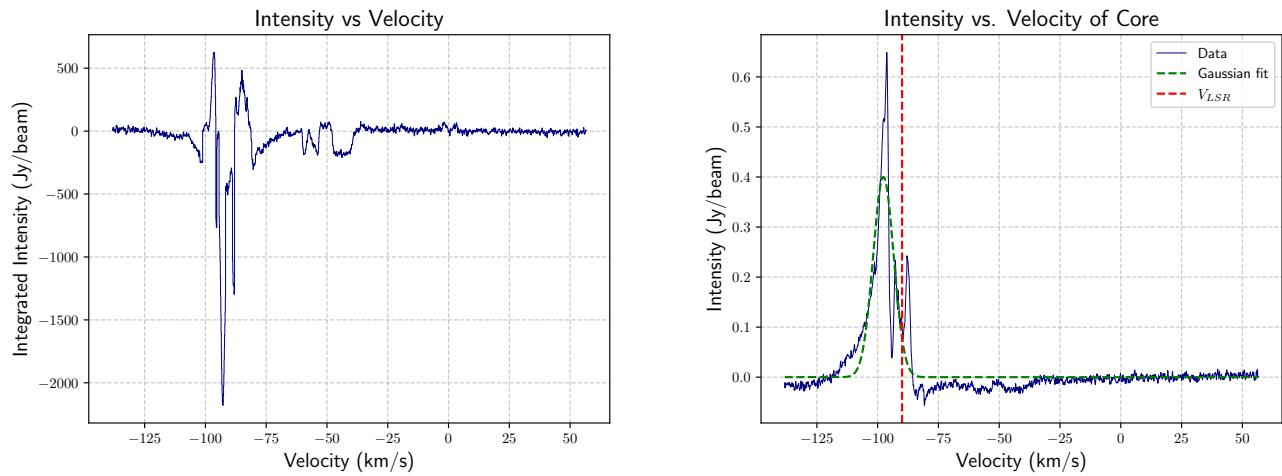
Figure 17



(a) Intensity vs. Velocity plot for the HII region containing the source IRAS 16060-5146 CO

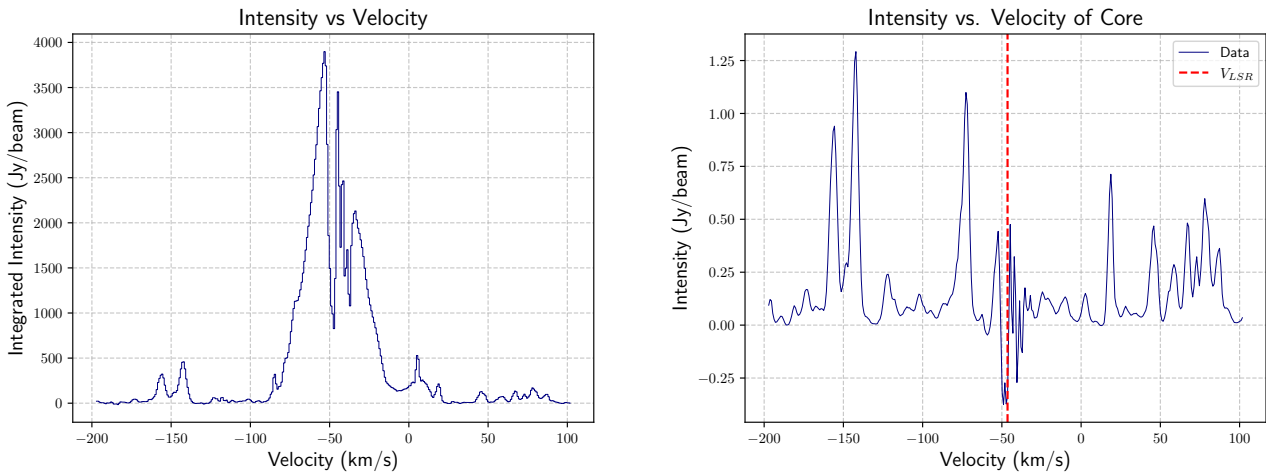
(b) Intensity vs. Velocity plot for the major star forming core in the HII region

Figure 18

(a) Intensity vs. Velocity plot for the HII region containing the source IRAS 16060-5146 HCO<sup>+</sup>

(b) Intensity vs. Velocity plot for the major star forming core in the HII region

Figure 19



(a) Intensity vs. Velocity plot for the HII region containing the source IRAS 16272-4837 CO (b) Intensity vs. Velocity plot for the major star forming core in the HII region

Figure 20

## 8.1 Position-Velocity Diagrams

Position-Velocity (PV) diagrams are employed to elucidate the structure of outflows. Typically, PV diagrams reveal a high-velocity region indicative of the original jet's velocity, characterized by a distinct profile along the velocity axis, and a lower-velocity region corresponding to the outflow, which tends to be more distributed along the position axis. Additionally, many PV diagrams prominently display knot-like structures, which offer valuable insights into the detailed morphology of the outflows.

The function `plot_pv_diagram` is designed to generate and visualize position-velocity (PV) diagrams from spectral data. This function takes several inputs, including the path to a FITS file, the name for the output file, the local standard of rest (LSR) velocity, a list of region files, the distance to the object in parsecs, and an optional boolean flag to save the figures.

The function begins by defining a fixed output path where results will be saved. It then iterates through each region file specified in

`path_reg_files`. For each file, it parses the region data, extracting coordinates of points which define the path along which the PV diagram will be extracted. These points are read from the region file and stored in a list. If no valid points are found, an error is raised.

A path width is defined to specify the thickness of the path in pixels. A `Path` object is created using the extracted points, which is used to extract the PV slice from the data cube.

Next, the function reads the FITS file specified by `pv_fits_file` using `SpectralCube.read`. It then determines the index corresponding to the LSR velocity in the spectral axis, and identifies the range around this velocity for extracting the PV slice. The velocity range is defined by a specified delta value, and the lower and upper bounds are calculated. If necessary, these bounds are swapped to ensure correct extraction.

A sub-cube is then extracted from the original data cube based on the calculated bounds. This sub-cube is further processed to extract the PV slice using the previously defined path. The dimensions of the resulting PV slice are logged.

The pixel scale is computed in arcseconds and converted to parsecs using the distance to the object. This allows the offset axis of the PV diagram to be represented in parsecs. The function also extracts velocity values corresponding to the frames within the specified range.

A plot of the PV diagram is generated with velocity on the y-axis and offset along the path on the x-axis. The plot uses a colormap to represent intensity. Additionally, the PV slice data is saved as a FITS file in the same directory.

The function also optionally saves the velocity values and corresponding intensities to a text file, providing a detailed record of the PV diagram data. This file is saved in the output directory, and its location is printed for reference.

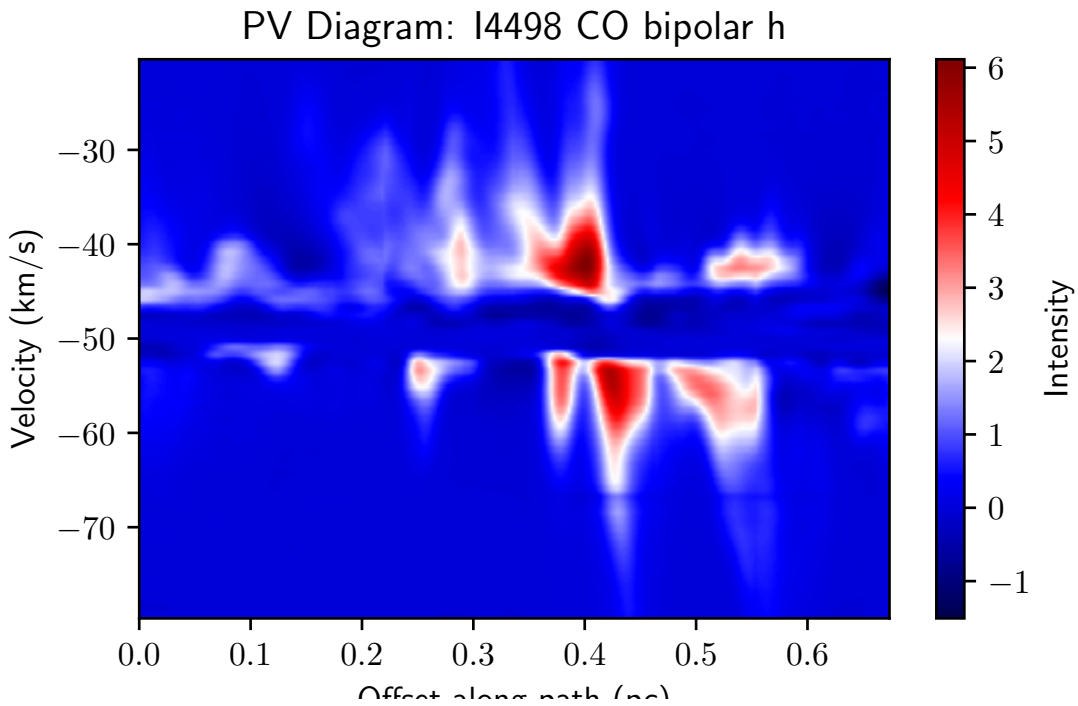


Figure 21: Position-velocity diagram for the source IRAS 14498-5856 CO showing the horizontal bipolar velocity structure.

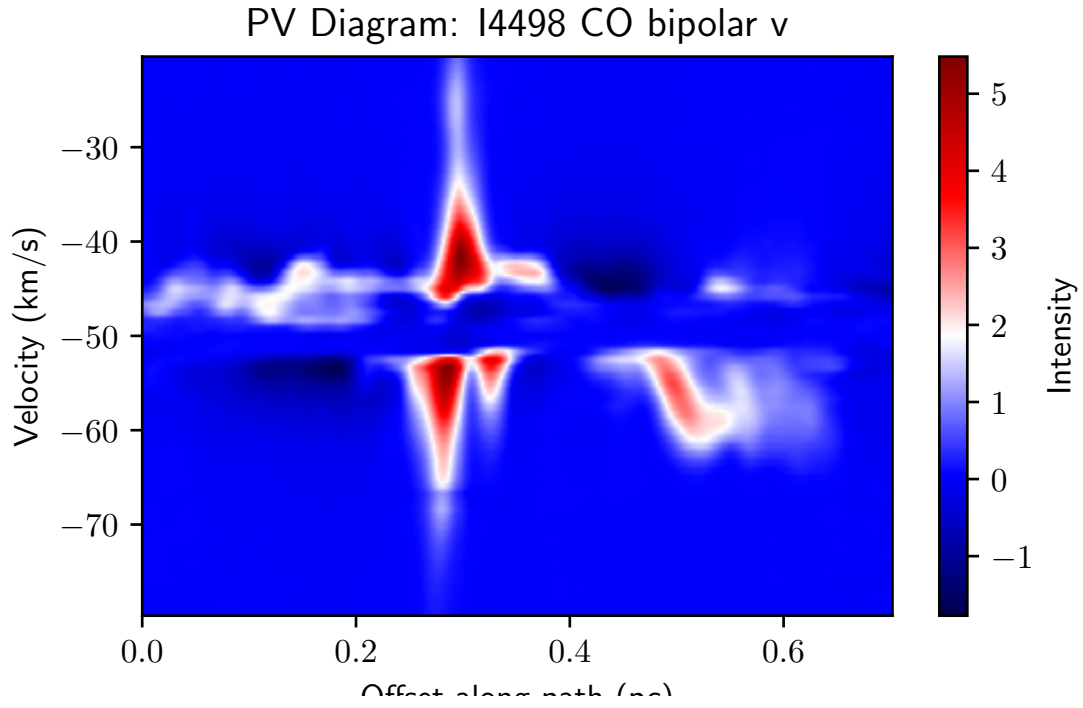


Figure 22: Position-velocity diagram for the source IRAS 14498-5856 CO showing the vertical bipolar velocity structure.

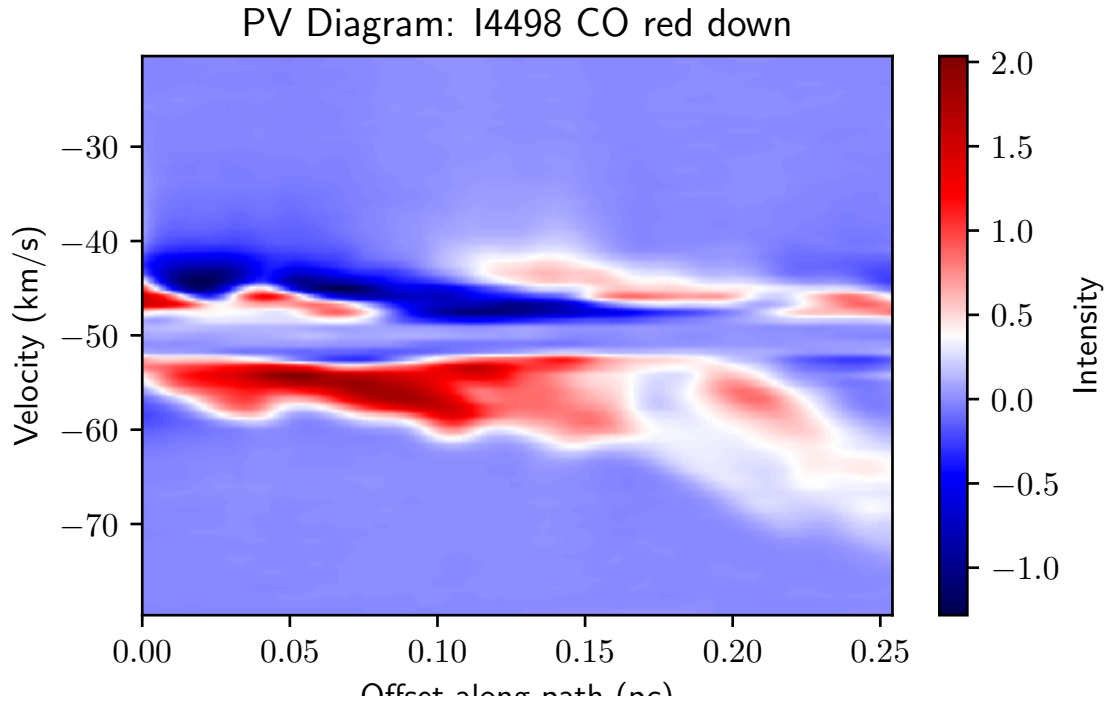


Figure 23: Position-velocity diagram for the source IRAS 14498-5856 CO showing the redshifted outflow below.

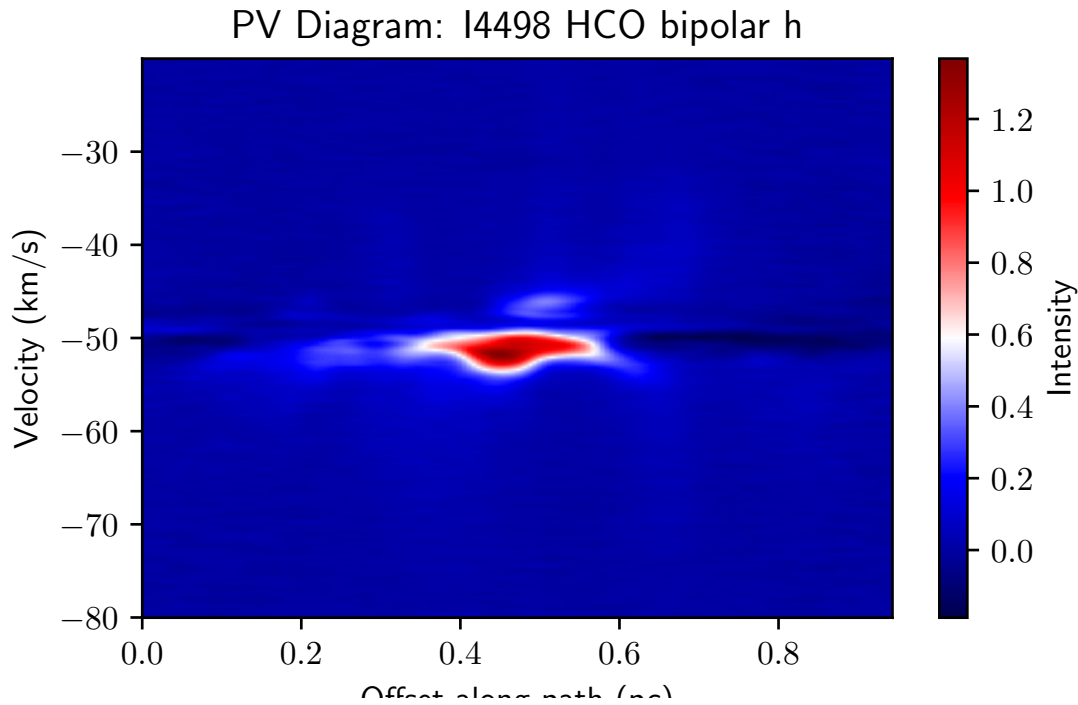


Figure 24: Position-velocity diagram of IRAS 14498-5856 HCO<sup>+</sup> showing the horizontal bipolar outflow structure

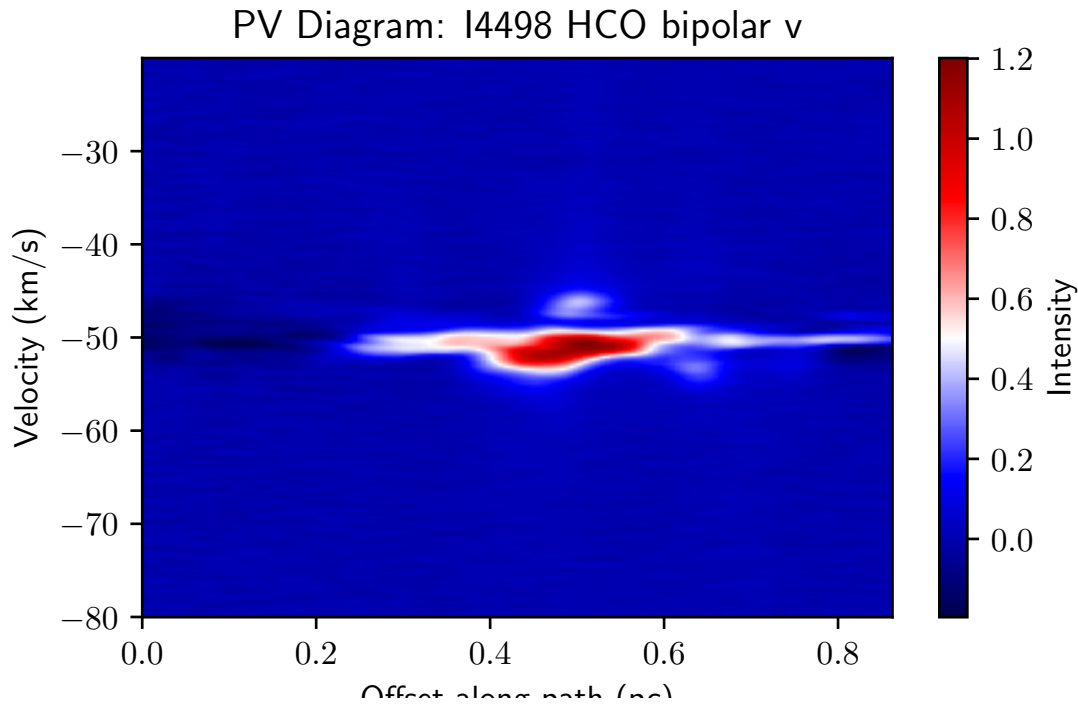


Figure 25: Position-velocity diagram of IRAS 14498-5856 HCO<sup>+</sup> showing the vertical bipolar outflow structure

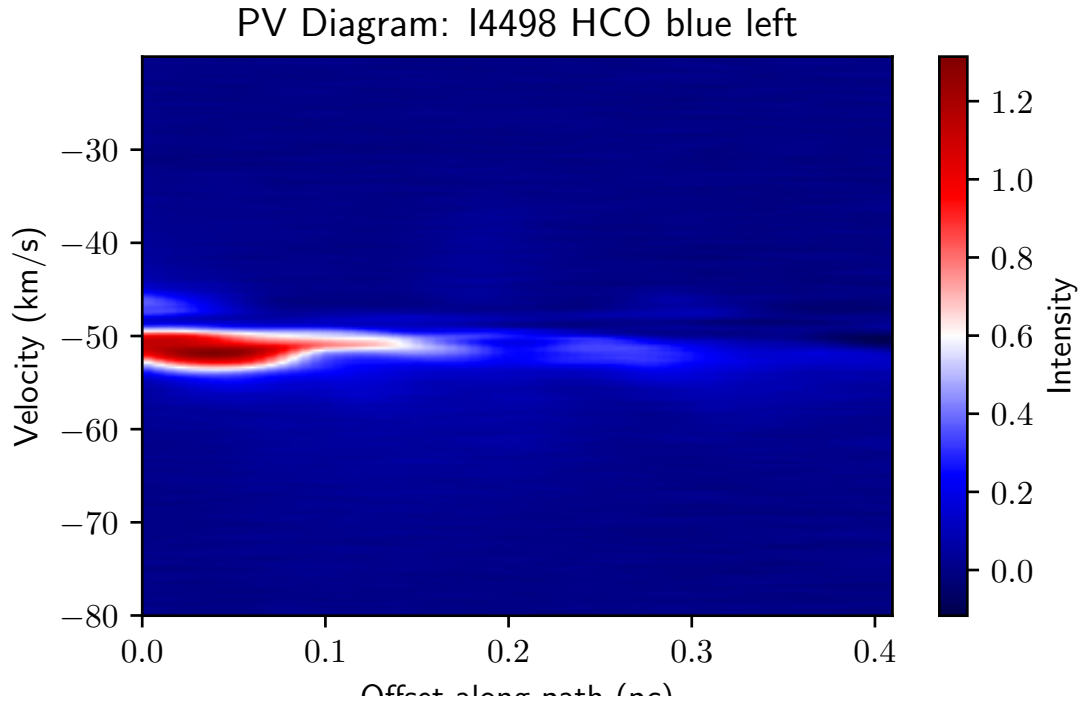


Figure 26: Position-velocity diagram depicting the blue-shifted outflow to the left of the source in IRAS 14498-5856 HCO<sup>+</sup>

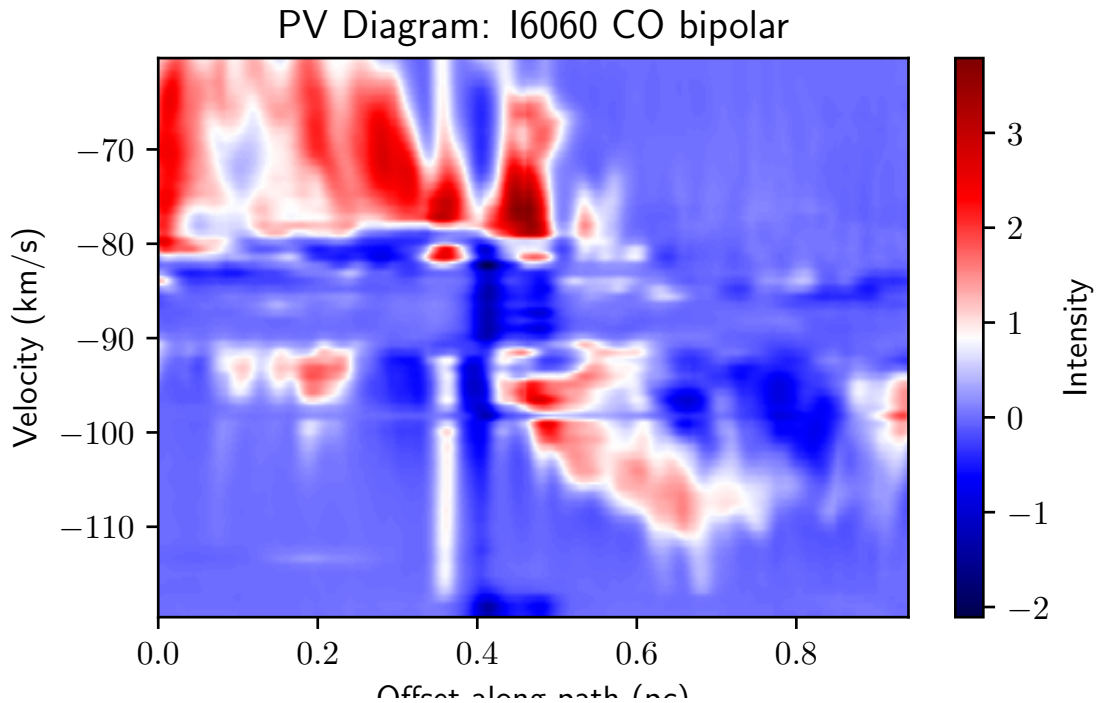


Figure 27: Position-velocity diagram of IRAS 16060-5146 CO showing the horizontal bipolar outflow structure

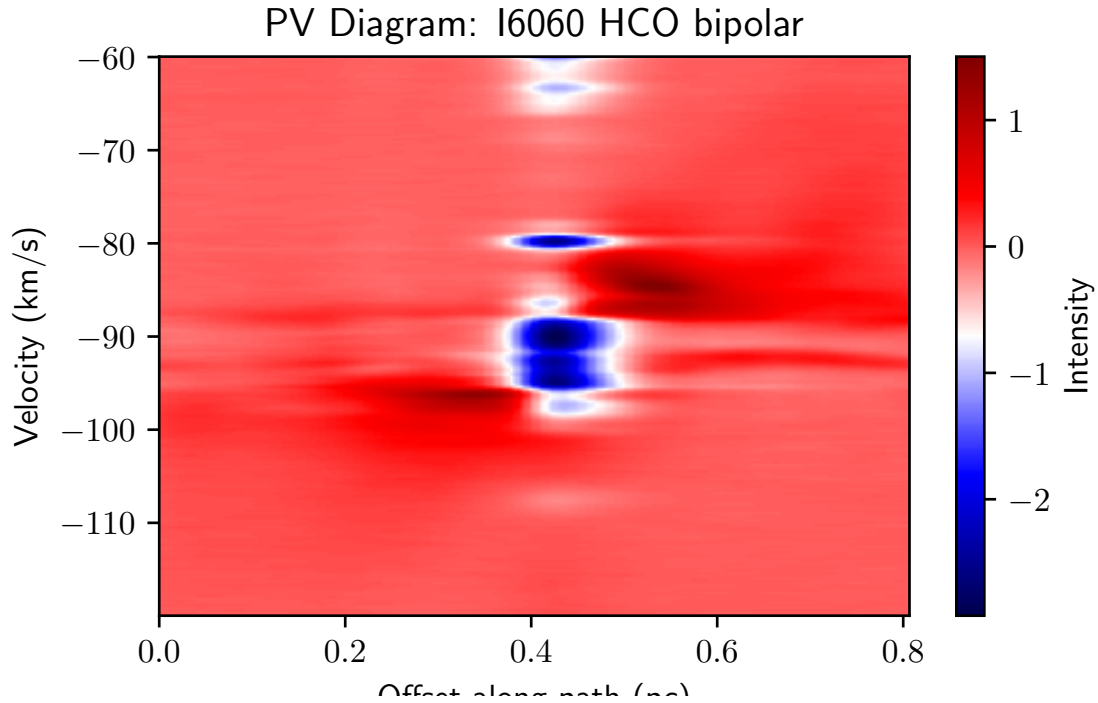


Figure 28: Position-velocity diagram of IRAS 16060-5146 HCO<sup>+</sup> showing the horizontal bipolar outflow structure. It must be noted that the central structure has unexpected low intensity due to over-subtraction in that region during data calibration.

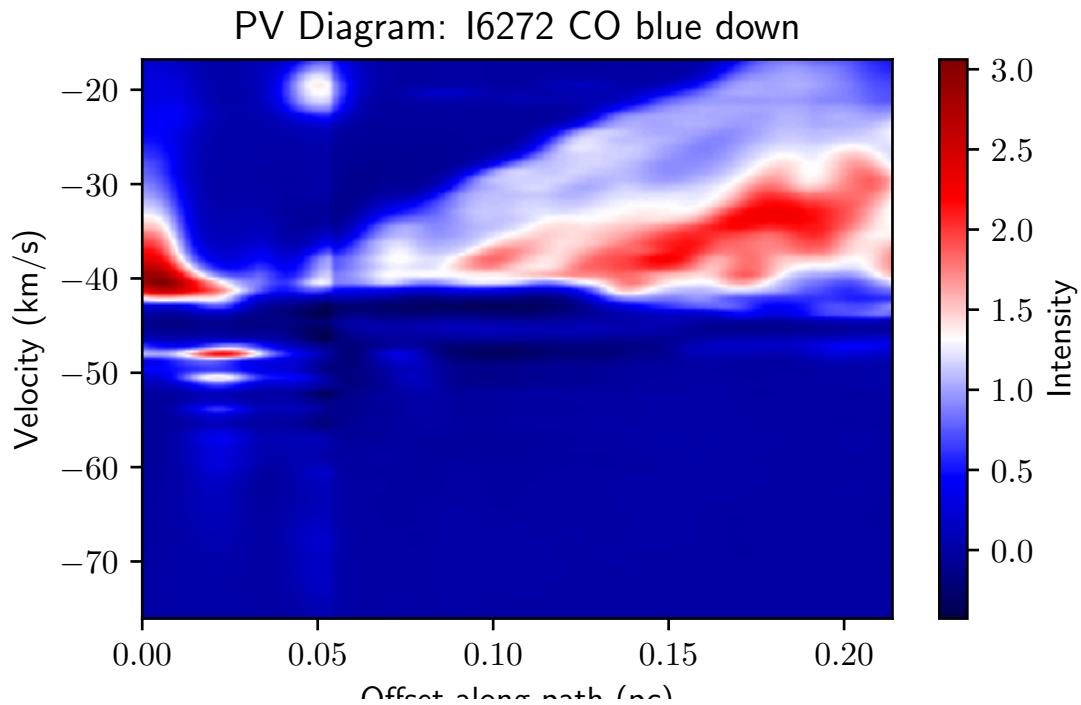


Figure 29: Position-velocity diagram of IRAS 16272-4837 CO showing the blue-shifted emission structure towards the south.

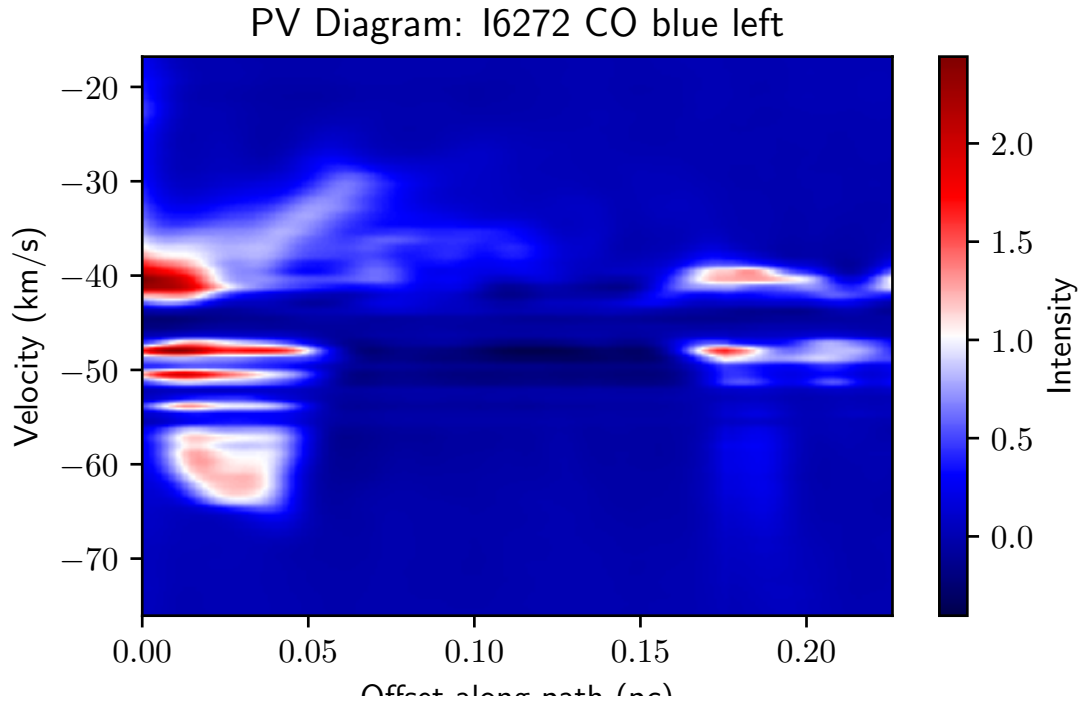


Figure 30: Position-velocity diagram of IRAS 16272-4837 CO showing the blue-shifted emission structure towards the left.

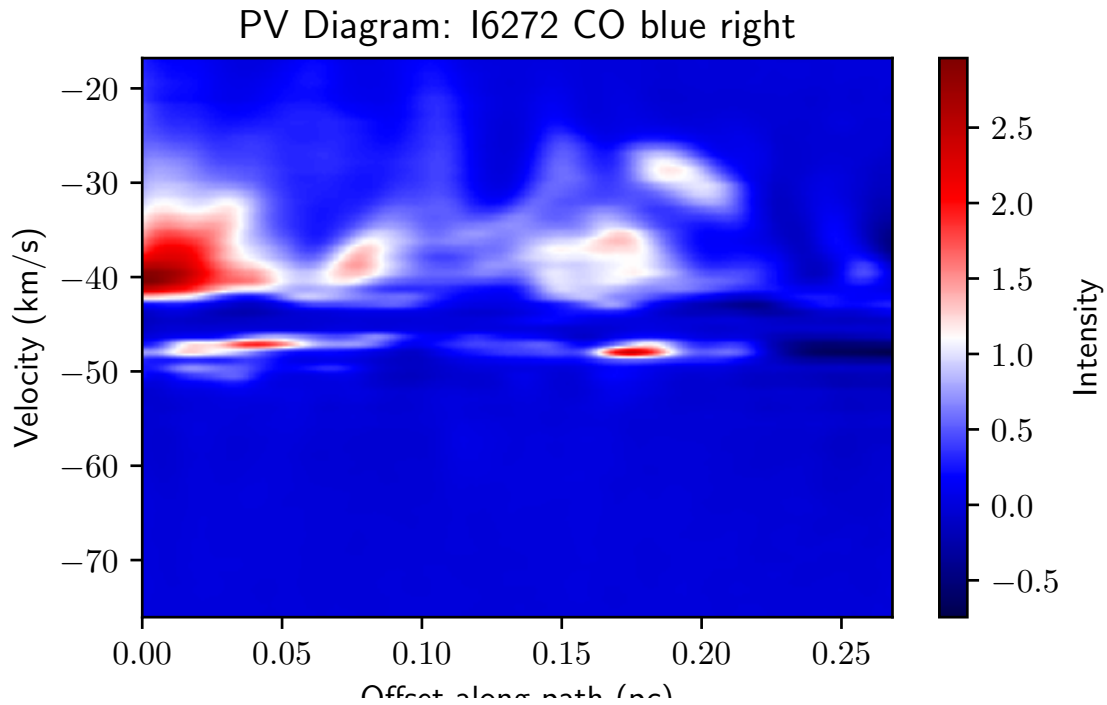


Figure 31: Position-velocity diagram of IRAS 16272-4837 CO showing the blue-shifted emission structure towards the right.

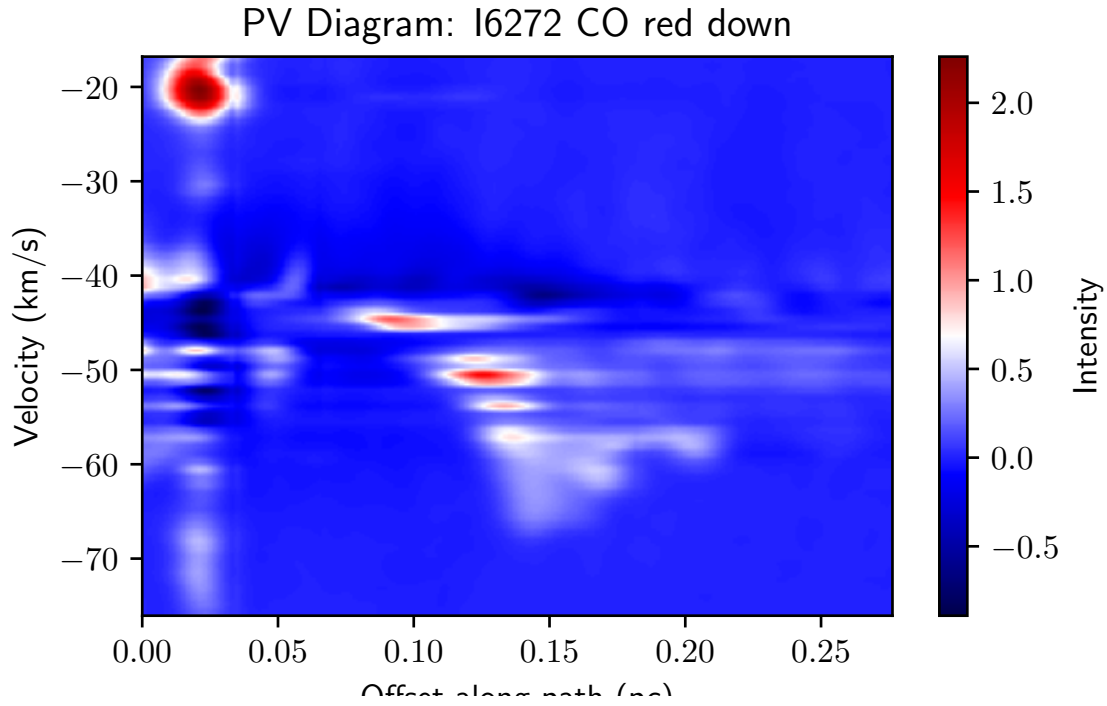


Figure 32: Position-velocity diagram of IRAS 16272-4837 CO showing the red-shifted emission structure towards the south.

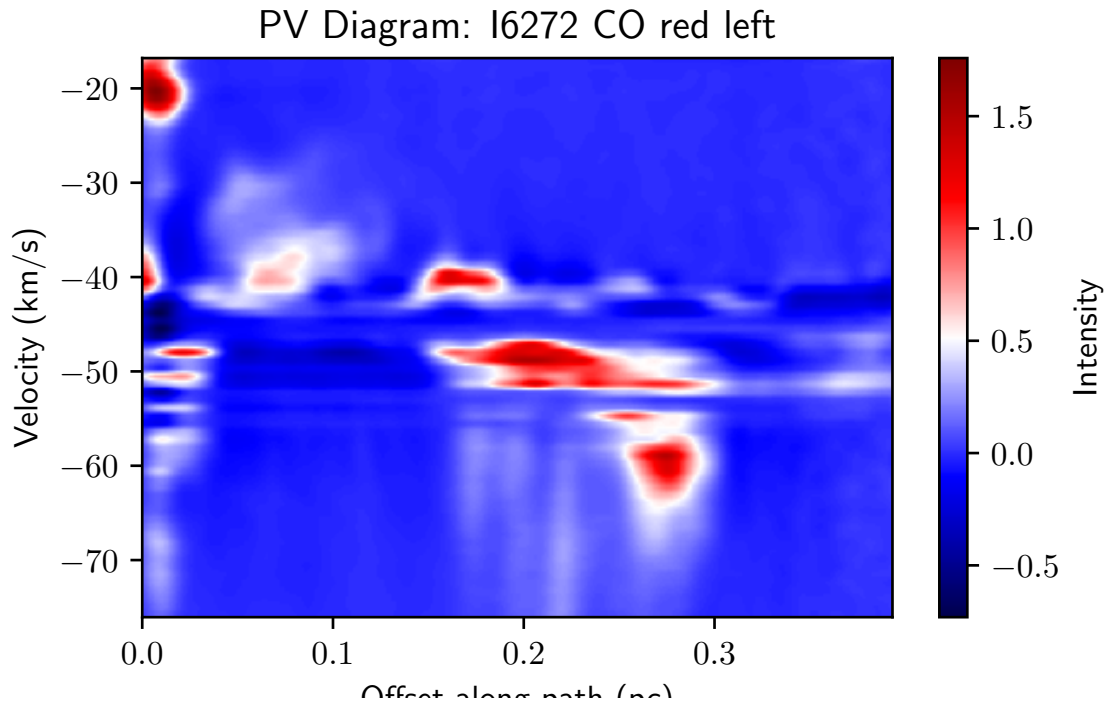


Figure 33: Position-velocity diagram of IRAS 16272-4837 CO showing the red-shifted emission structure towards the left.

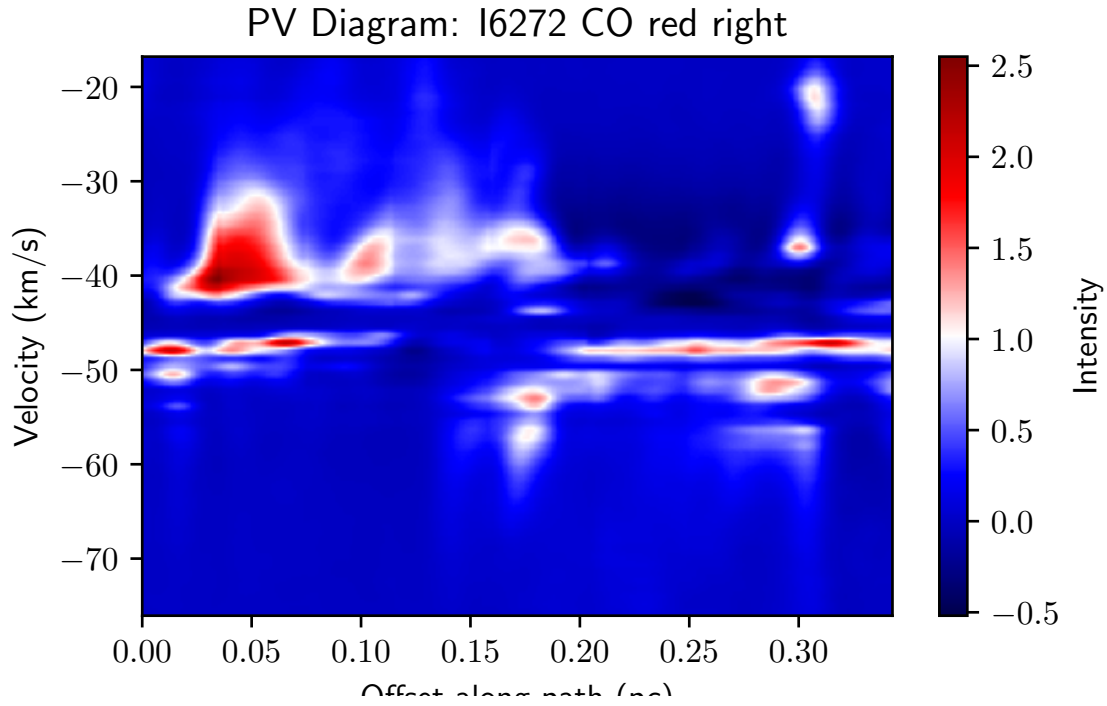


Figure 34: Position-velocity diagram of IRAS 16272-4837 CO showing the red-shifted emission structure towards the right.

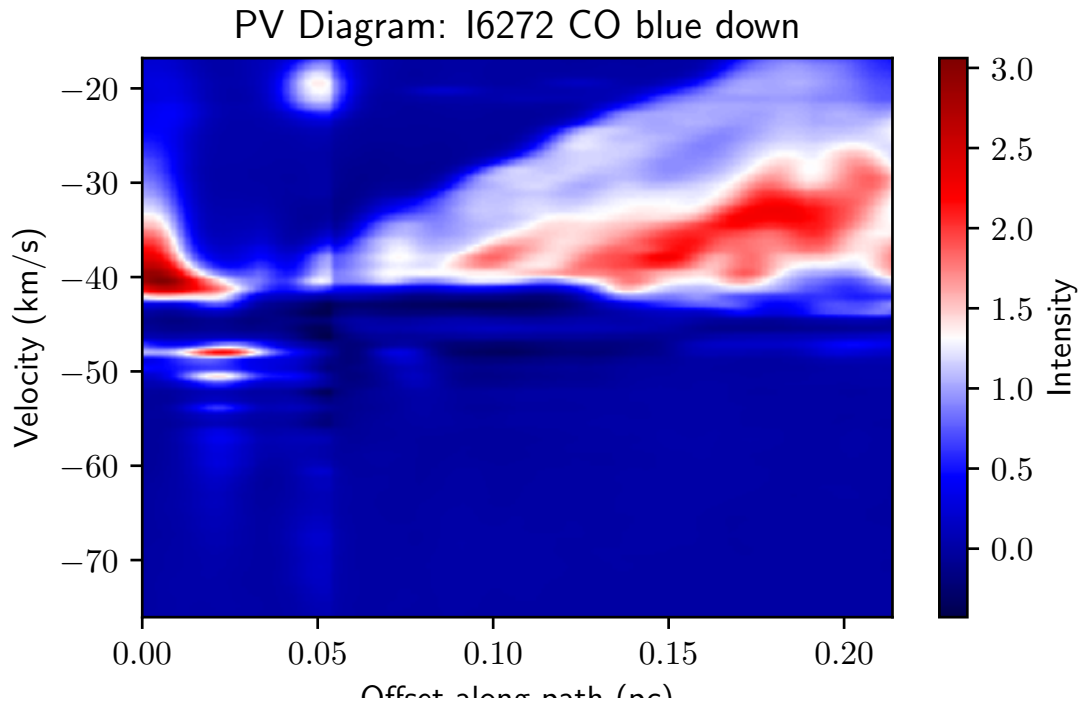


Figure 35: Position-velocity diagram of IRAS 16272-4837 CO showing the blue-shifted emission structure towards the south.

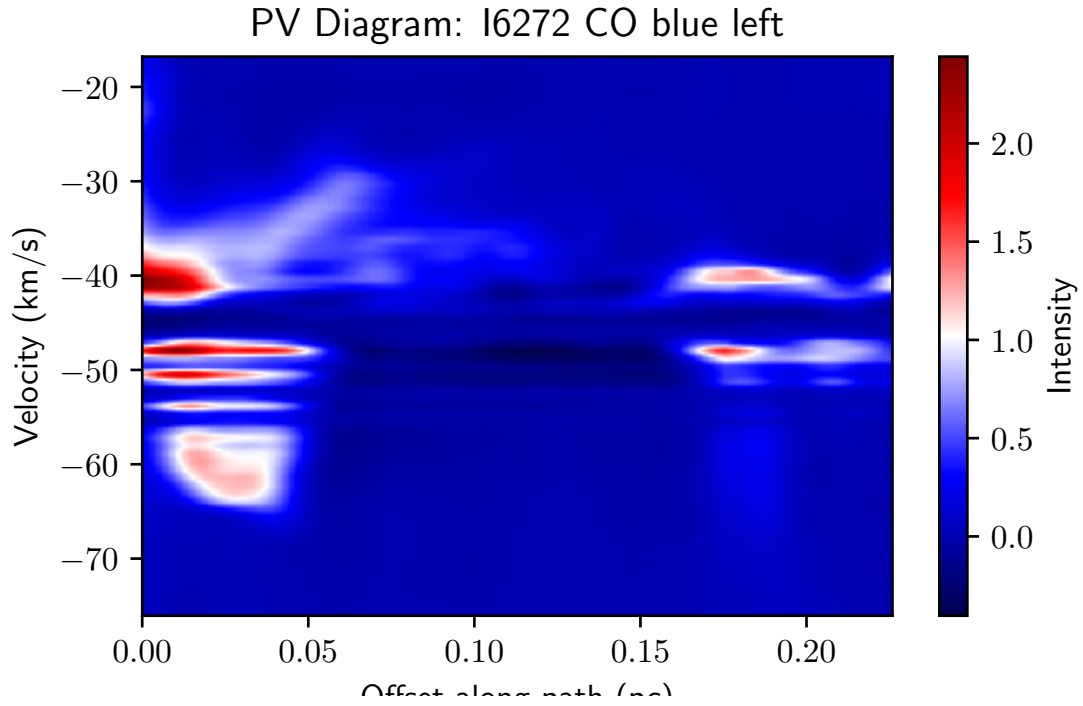


Figure 36: Position-velocity diagram of IRAS 16272-4837 CO showing the blue-shifted emission structure towards the left.

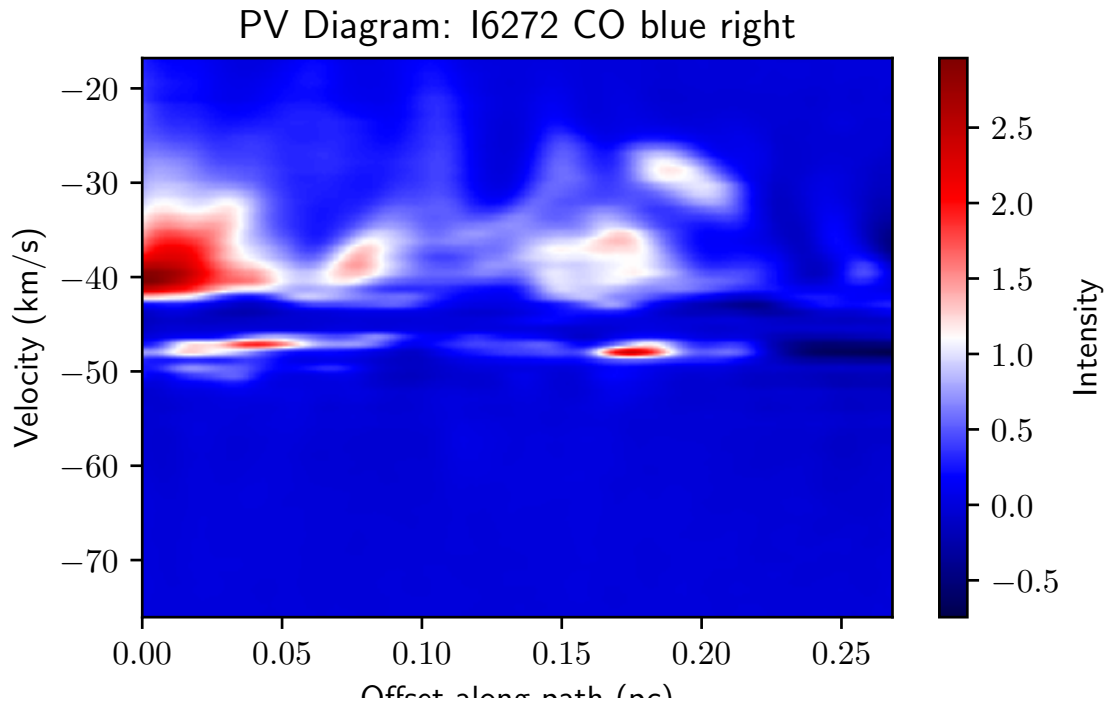


Figure 37: Position-velocity diagram of IRAS 16272-4837 CO showing the blue-shifted emission structure towards the right.

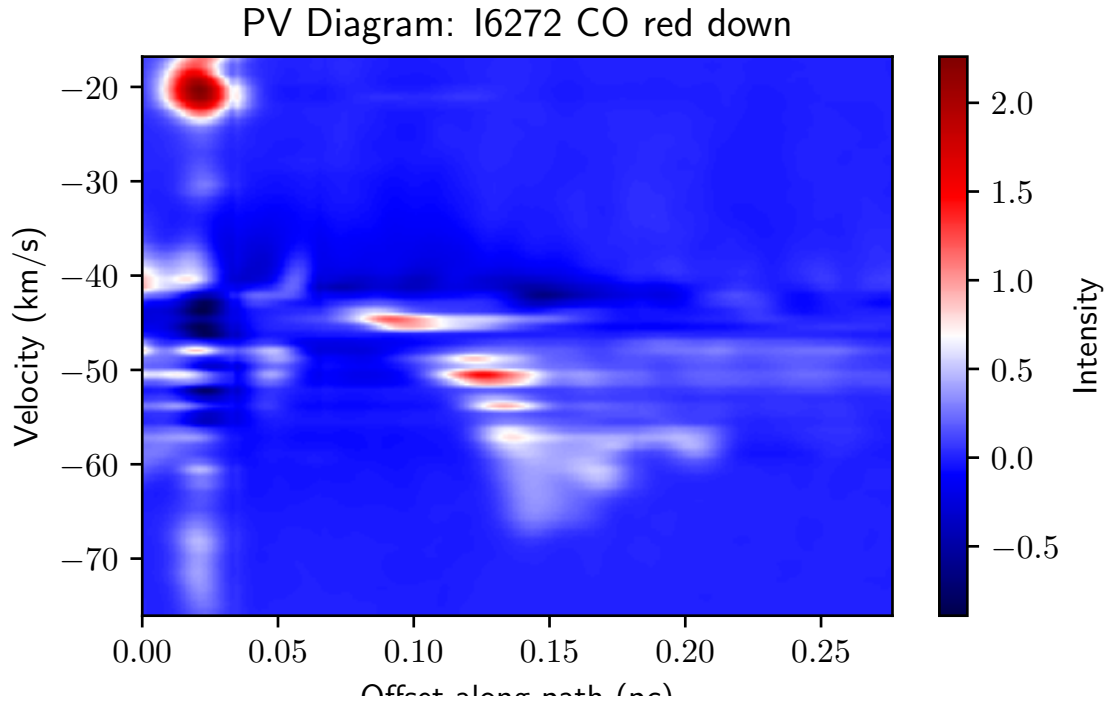


Figure 38: Position-velocity diagram of IRAS 16272-4837 CO showing the red-shifted emission structure towards the south.

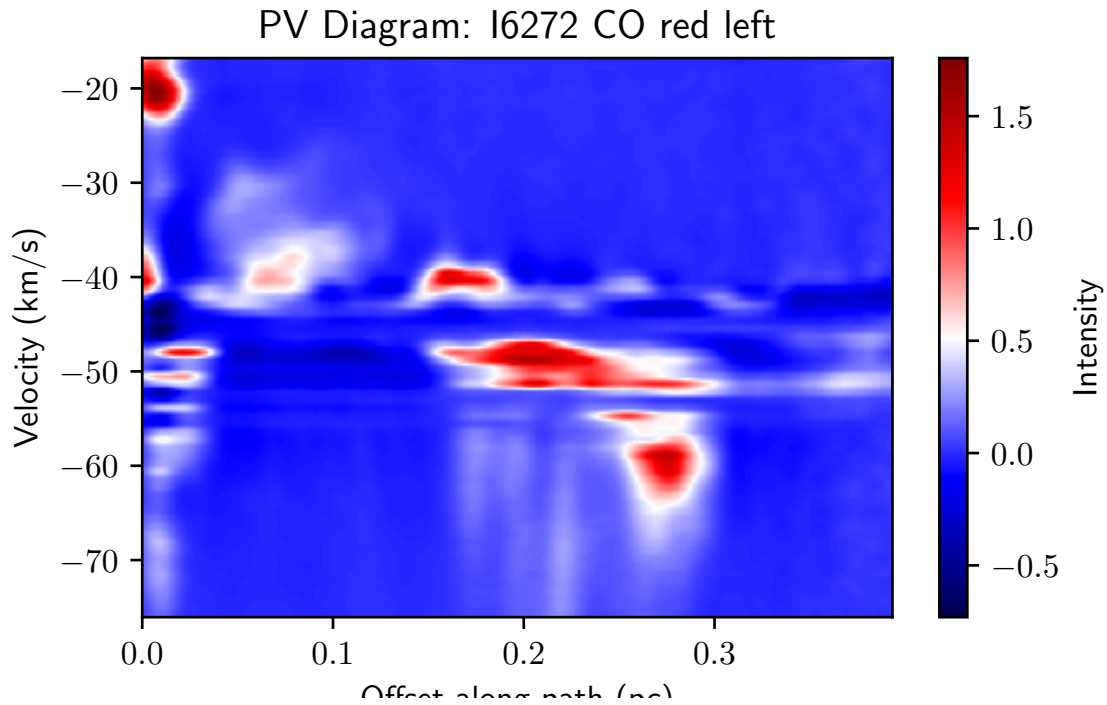


Figure 39: Position-velocity diagram of IRAS 16272-4837 CO showing the red-shifted emission structure towards the left.

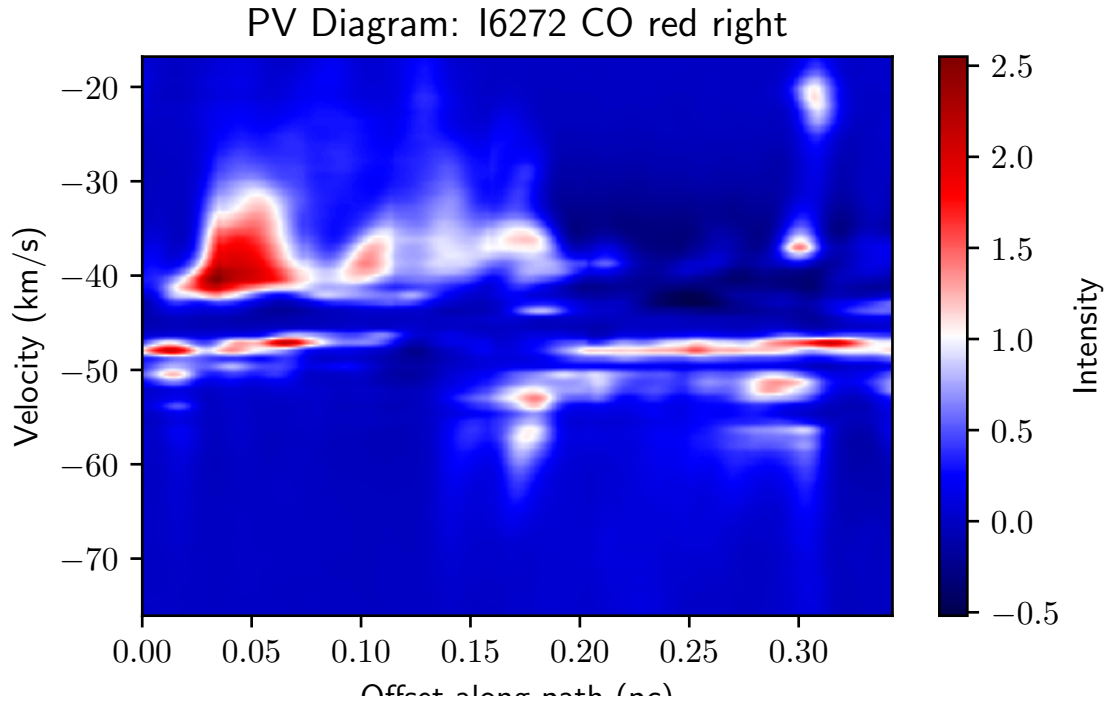


Figure 40: Position-velocity diagram of IRAS 16272-48376 CO showing the red-shifted emission structure towards the right.

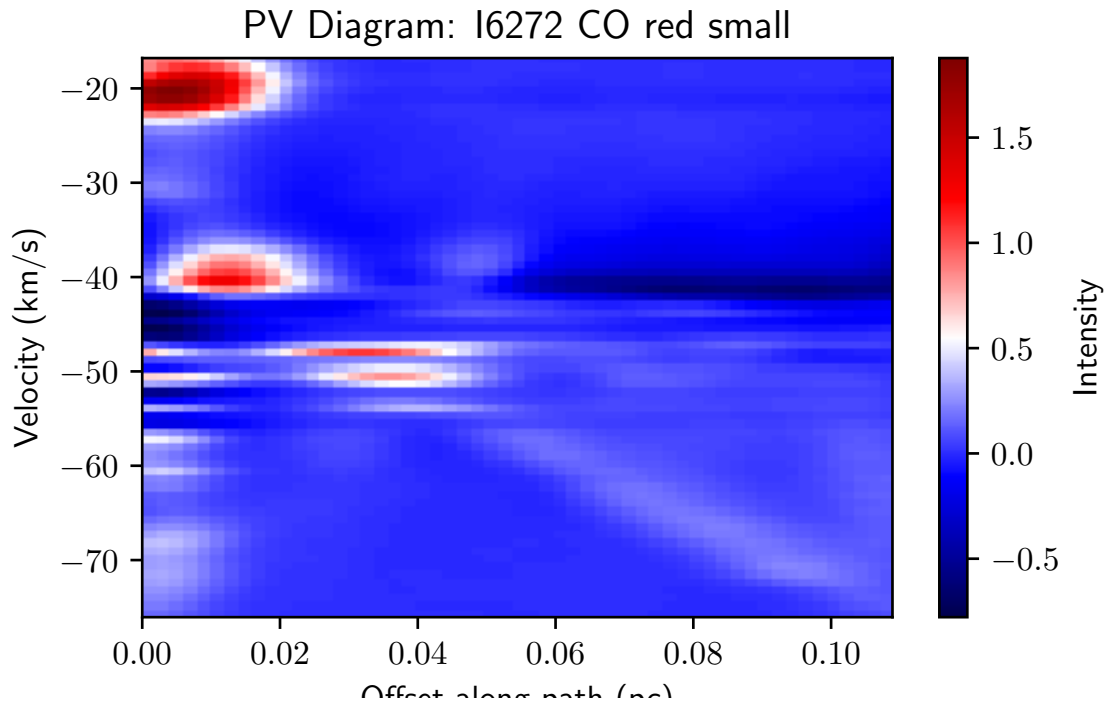


Figure 41: Position-velocity diagram of IRAS 16272-4837 CO highlighting the compact red-shifted emission feature towards the right.

## 8.2 Estimation of Outflow Parameters

### 8.2 Core Identification

Identifying star-forming cores is crucial for understanding protostellar outflows. The `astrodendro` package offers a straightforward method for computing dendrograms from observed or simulated astronomical data in Python, making it suitable for identifying these cores, which are characterized by high intensity across multiple channels. This analysis requires continuum data, and thus was only performed for two CO sources, as continuum data for other sources was unavailable.

The provided code conducts an analysis of astronomical data from a FITS (Flexible Image Transport System) file to extract and compute the physical properties of identified sources. The primary objective is to calculate the mass of these sources based on their observed intensity and subsequently generate output files containing detailed information about each source.

Initially, the code defines several constants relevant to astronomical calculations, including the speed of light, Planck constant, Boltzmann constant, and the conversion factor for parsecs to centimeters. These constants are crucial for accurately computing physical quantities from observational data.

The `planck` function is then defined to compute the Planck function, which describes the intensity of radiation from a blackbody at a specific frequency (`nu`) and temperature (`Temp`). This function determines the wavelength from the frequency, computes intermediate values, and then calculates the intensity of the radiation.

Following this, the `CalculateMassFromIntensity` function is used to compute the mass of an astronomical source based on its intensity. This function requires several parameters, including the dust temperature (`Tdust`), frequency (`nu`), observed flux density (`Fnu`), distance to the source (`dist`), and spectral index (`beta`). It converts the distance from kiloparsecs to centimeters and computes the opacity (`kappa`) based on the spectral index. The function then calculates the flux in Jansky and uses the Planck function to determine the mass of the source, which is returned in solar masses.

The `process_fits_file` function performs the core analysis. It starts by defining parameters used for processing the FITS file, such as dust temperature, gas-to-dust ratio, and statistical thresholds. The FITS file is opened to extract the relevant header and data information, with the observing frequency read from the FITS header.

The function then calculates the pixel size and the width of the celestial coordinates. It uses this information to determine the size of the field of view in pixels and retrieves the beam's major and minor axes. These measurements are vital for assessing the spatial properties of the detected sources.

The `Dendrogram.compute` method is then employed to analyze the data and identify sources based on predefined thresholds. A dendrogram, which is a hierarchical structure, aids in identifying and classifying objects within the data.

Subsequently, the function ensures that necessary directories for saving output files are present,

creating them if they do not exist. Three output files are opened to save detailed source information, regions in DS9 format, and CASA region files.

For each identified source, the function extracts properties such as position, flux, and size, and calculates the source's mass using the `CalculateMassFromIntensity` function with two different spectral indices. The results, including coordinates, size, flux, and mass, are written to the output files. These files are formatted to facilitate visualization and further analysis in tools such as DS9 and CASA.

Finally, the function outputs the number of selected sources, summarizing the detected objects and their computed properties.

RA	Dec	FWHMx (")	FWHMy (")	PA	R (")	Area (sq-")	Flux (Jy)	$M_{\odot}$ $\beta = 1.5$	$M_{\odot}$ $\beta = 2$
223.427987	-59.147998	2.226	1.225	154.52	1.652	11.222	1.8913e+00	117.34	$\beta = 1.5$

Table 2: Summary of Calculated properties of the star forming core in IRAS 14498-5856

RA	Dec	FWHMx (")	FWHMy (")	PA	R (")	Area (sq-")	Flux (Jy)	$M_{\odot}$ $\beta = 1.5$	$M_{\odot}$ $\beta = 2$
242.468543	-51.915496	0.897	0.622	72.39	0.747	1.943	3.1577e+00	517.34	951.96
242.469311	-51.915121	1.664	1.359	-152.71	1.504	6.726	1.2558e+01	2057.34	3785.74

Table 3: Summary of Calculated properties of the star forming cores in IRAS 16060-5146

Finally, the function outputs the number of selected sources, summarizing the detected objects and their computed properties.

## 8.2 Temperature

Temperature in molecular clouds can be calculated by comparing the intensities of two spectral lines from the same species but corresponding to different transitions. This method leverages the fact that the population levels of the molecule, which are assumed to be in thermal equilibrium, follow a Boltzmann distribution. By comparing the intensities of these transitions, the excitation temperature, which reflects the thermal conditions of the gas, can be derived. This approach is particularly useful for understanding the physical state of interstellar gas where direct temperature measurements are challenging.

In this work, a function was developed to calculate the excitation temperature by comparing the intensities of two spectral lines corresponding to different transitions of the HCO<sup>+</sup> molecule, specifically the (4-3) and (1-0) transitions. The function, named `excitation_temperature`, automates the process of extracting the necessary data from FITS files and performing the temperature calculation. This couldn't be done for the CO data as information from 2 transitions wasn't available.

The `excitation_temperature` function begins by reading the headers of the FITS files using the `read_fits_header` function. This step extracts essential observational parameters such as the

rest frequencies (`nu_1` for the (1-0) transition and `nu_2` for the (4-3) transition), right ascension (`ra_1` and `ra_2`), declination (`dec_1` and `dec_2`), and the beam area in steradians (`beam_area_sr_1` and `beam_area_sr_2`). These parameters are crucial for ensuring the consistency and accuracy of the subsequent calculations.

To validate that the data corresponds to the same region of space, the function checks that the right ascension and declination values are consistent across both FITS files. This is particularly important since the calculations assume that the observed region is identical for both transitions.

Next, the spectral data for each transition are extracted using the `extract_spectrum` function, which retrieves the intensity and velocity arrays based on the specified coordinates. The intensity values are then integrated over the velocity axis using the `integrate_intensity` function, which employs the trapezoidal rule (via `np.trapz`) to approximate the total emission in units of Jy/beam \* km/s.

The integrated intensities, initially in units of Jy/beam, are then converted to W/m<sup>2</sup>/Hz using the `convert_jy_per_beam_to_w_per_m2_hz` function. This conversion accounts for the beam area in steradians, ensuring that the intensity values are expressed in consistent physical units necessary for accurate temperature calculation.

Finally, the excitation temperature is computed using the formula:

$$T_{\text{ex}} = \frac{E_2 - E_1}{k \ln \left( \frac{I_1}{I_2} \right)}$$

where  $E_1$  and  $E_2$  are the energies associated with the transitions (1-0) and (4-3), respectively,  $I_1$  and  $I_2$  are the integrated intensities,  $\nu_1$  and  $\nu_2$  are the respective frequencies, and  $k$  is the Boltzmann constant. This equation, implemented within the `calculate_excitation_temperature` function, relies on the logarithmic ratio of the intensity values, adjusted for the difference in frequency, to derive the excitation temperature.

Two methods were employed in this as well. In the first method, the entire data cube was used in the calculation and in the second method only the peak around  $V_{LSR}$  was considered. Using these methods, the temperature values were obtained as:

IRAS 14498-5856: 0.492 K, 0.493 K (using peak only)  
 IRAS 16060-5146: 8.757 K, 77.669 K (using peak only)

## 8.2 Dynamical Properties of Outflows

Calculating the dynamical properties of CO outflows is essential for understanding the dynamics and evolution of massive star-forming regions. Parameters such as mass, momentum, energy, dynamical time, and outflow rate are critical for characterizing the physical conditions and processes within these regions.

Central to this analysis is the accurate estimation of the CO column density ( $N_{\text{CO}}$ ), which is fundamental for deriving the other dynamical properties. The CO column density is computed using the following formula [5]:

$$N_{\text{CO}}(\text{cm}^{-2}) = 4.81 \times 10^{12} \times (T_{\text{ex}} + 0.92) \times \exp\left(\frac{33.12}{T_{\text{ex}}}\right) \times T_B \times dv$$

where  $T_{\text{ex}}$  represents the excitation temperature,  $T_B$  denotes the brightness temperature, and  $dv$  is the velocity channel width in km/s. This equation, derived from radiative transfer models under the assumption of optically thin conditions, is crucial for estimating  $N_{\text{CO}}$ , particularly in massive star-forming regions where CO is abundant and plays a significant role in cooling the gas.

An excitation temperature ( $T_{\text{ex}}$ ) of 50 K is assumed, which is a reasonable estimate for the warm molecular gas associated with H II regions in massive star-forming environments. This assumption simplifies the calculation, though it is acknowledged that  $T_{\text{ex}}$  may vary spatially across the outflows, potentially introducing some uncertainties into the derived parameters. However, given that low-J transitions of CO, such as those employed in this study, are generally insensitive to temperatures above 50 K, this assumption remains robust for the analysis.

Once  $N_{\text{CO}}$  is estimated, it is used to calculate the molecular hydrogen column density ( $N_{\text{H}_2}$ ) by assuming a fixed CO-to-H<sub>2</sub> abundance ratio. The mass, momentum, and energy of the outflows are then derived from these column densities, in conjunction with the velocity information obtained from the spectral data.

A Python code has been developed to calculate the dynamical properties of CO outflows from observational data. The code operates through several steps, each corresponding to different aspects of data processing and parameter estimation.

The code begins by defining various constants and coefficients required for the calculations. This includes conversion factors for distance (from parsecs to centimeters), time (from years to seconds), and mass (from solar masses to grams). Specific coefficients  $A$  and  $B$  for different CO transitions (1-0, 2-1, 3-2, 4-3) are also defined based on radiative transfer models. These coefficients are used in the formula for calculating the CO column density.

The `PerFrameMassMomentumEnergy` function calculates the mass, momentum, and energy for each velocity channel within a specified region of the outflow. The function converts angular sizes from the spectral cube into physical dimensions, computes the CO column density using the aforementioned formula, and then scales this to the hydrogen column density. From these densities, the function computes the mass (in solar masses), momentum (in solar mass km/s), and energy (in Joules) of the outflow using the following formulas:

The total mass of the outflow is calculated using the formula [5]:

$$M_{\text{out}} = \frac{d^2}{\text{CO}} \int N_{\text{CO}} d\Omega$$

where  $d$  represents the distance to the source, and CO is the conversion factor for the CO column density.

The total momentum of the outflow is given by [5]:

$$P_{\text{out}} = M_{\text{out}} \times v$$

where  $v$  is the velocity of the outflow.

The total energy associated with the outflow is [5]::

$$E_{\text{out}} = \frac{1}{2} M_{\text{out}} v^2$$

The `Cal_DynAge_OutflowRate` function calculates the dynamical age (time required for the outflow to reach its current size) and the outflow rate (mass loss rate) using the following formulas:

The dynamical time,  $t_{\text{dyn}}$ , is computed as:

$$t_{\text{dyn}} = \frac{L_{\text{flow}}}{v}$$

where  $L_{\text{flow}}$  represents the length of the outflow, and  $v$  is the outflow velocity.

The mass outflow rate is determined by [5]:

$$\dot{M}_{\text{out}} = \frac{M_{\text{out}}}{t_{\text{dyn}}}$$

The `Cal_CO_Mass_Momentum_Energy` function processes the spectral data cube, which contains velocity-resolved CO emission. It uses a World Coordinate System (WCS) to convert pixel coordinates to physical coordinates, enabling the integration of emission over specific velocity ranges. This function iterates over the selected velocity channels, applies a region mask to isolate the outflow, and calculates the total mass, momentum, and energy by summing the contributions from each channel. The intensity in Jy/beam from the original data cubes is converted to brightness temperature.

The `calculate_length` function estimates the physical length of the outflow lobes based on the angular separation between two points defined in a region file. This length is crucial for determining the dynamical time and outflow rate.

The main loop iterates over predefined regions corresponding to different outflow lobes, calculating the relevant dynamical properties for each lobe. For each region, the spectral data is processed, and the mass, momentum, energy, dynamical time, and outflow rate are printed. These outputs provide insights into the physical state of the outflows in the target region.

Outflow Lobe	Direction	$V_{\text{start}}$ (km/s)	$V_{\text{end}}$ (km/s)	Outflow Length (pc)	Mass ( $M_{\odot}$ )	Momentum ( $M_{\odot}$ km/s)	Energy (J)	Dynamical Time (yrs)	Outflow Rate ( $M_{\odot}/\text{yr}$ )
IRAS 14498-5856 O1	Blue	4.263	70.305	0.7984	$2.563 \times 10^{-1}$	$4.205 \times 10^1$	$6.872 \times 10^{42}$	11110.4	$2.307 \times 10^{-5}$
IRAS 14498-5856 O2	Blue	5.110	70.305	0.5349	$9.815 \times 10^{-2}$	$1.612 \times 10^1$	$2.639 \times 10^{42}$	7443.0	$1.319 \times 10^{-5}$
IRAS 14498-5856 O3	Red	1.663	17.750	0.4103	$3.474 \times 10^{-2}$	$4.953 \times 10^0$	$7.025 \times 10^{41}$	22615.7	$1.536 \times 10^{-6}$
IRAS 14498-5856 O4	Red	1.663	28.757	0.2280	$6.391 \times 10^{-2}$	$8.995 \times 10^0$	$1.260 \times 10^{42}$	7756.2	$8.240 \times 10^{-6}$
IRAS 14498-5856 O5	Red	2.510	83.792	0.6489	$1.820 \times 10^{-1}$	$2.577 \times 10^1$	$3.638 \times 10^{42}$	7576.6	$2.402 \times 10^{-5}$
IRAS 14498-5856 O6	Red	2.510	25.371	0.2161	$2.997 \times 10^{-2}$	$4.291 \times 10^0$	$6.114 \times 10^{41}$	8332.6	$3.596 \times 10^{-6}$
IRAS 14498-5856 O7	Red	2.510	27.064	0.1535	$1.170 \times 10^{-2}$	$1.670 \times 10^0$	$2.372 \times 10^{41}$	5549.0	$2.108 \times 10^{-6}$
IRAS 16060-5146 O1	Blue	9.313	49.951	0.8782	$2.316 \times 10^0$	$4.109 \times 10^2$	$7.260 \times 10^{43}$	17199.8	$1.347 \times 10^{-4}$
IRAS 16060-5146 O2	Red	27.939	3.386	0.8682	$1.538 \times 10^0$	$2.139 \times 10^2$	$2.903 \times 10^{43}$	30402.7	$5.059 \times 10^{-5}$
IRAS 16272-4837 O1	Blue	4.233	24.552	0.3062	$5.292 \times 10^{-2}$	$8.501 \times 10^0$	$1.359 \times 10^{42}$	12199.7	$4.337 \times 10^{-6}$
IRAS 16272-4837 O2	Blue	3.386	51.644	0.4646	$3.074 \times 10^{-1}$	$5.053 \times 10^1$	$8.278 \times 10^{42}$	8800.7	$3.493 \times 10^{-5}$
IRAS 16272-4837 O3	Blue	2.540	43.178	0.2443	$2.987 \times 10^{-1}$	$4.896 \times 10^1$	$7.997 \times 10^{42}$	5535.7	$5.395 \times 10^{-5}$
IRAS 16272-4837 O4	Red	44.871	0.847	0.5878	$1.440 \times 10^{-1}$	$2.016 \times 10^1$	$2.816 \times 10^{42}$	12816.8	$1.124 \times 10^{-5}$
IRAS 16272-4837 O5	Red	64.344	0.000	0.4040	$2.889 \times 10^{-1}$	$3.891 \times 10^1$	$5.239 \times 10^{42}$	6142.1	$4.703 \times 10^{-5}$
IRAS 16272-4837 O6	Red	44.871	0.000	0.4584	$5.545 \times 10^{-2}$	$7.708 \times 10^0$	$1.069 \times 10^{42}$	9994.8	$5.548 \times 10^{-6}$
IRAS 16272-4837 O7	Red	30.479	0.847	0.1666	$6.832 \times 10^{-3}$	$9.293 \times 10^{-1}$	$1.262 \times 10^{41}$	5346.5	$1.278 \times 10^{-6}$
IRAS 16272-4837 O8	Red	22.859	0.847	0.3489	$1.542 \times 10^{-2}$	$2.164 \times 10^0$	$3.024 \times 10^{41}$	14932.4	$1.033 \times 10^{-6}$

Table 4: Summary of Calculated dynamical properties of the outflows. The velocities are calculated with respect to the local standard of rest.

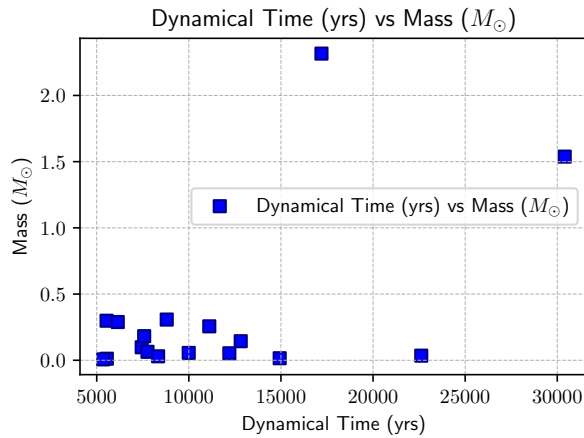


Figure 42: Correlation between outflow dynamical time and mass.

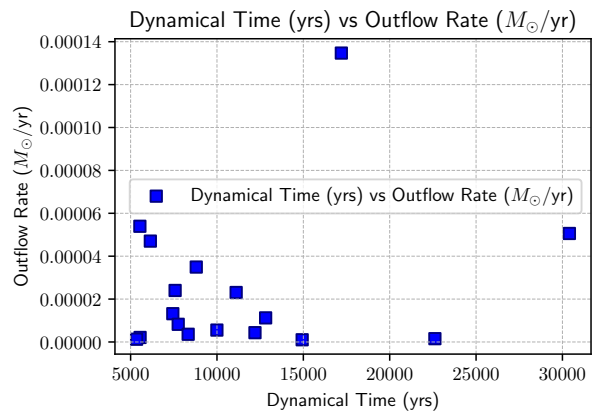


Figure 43: Relationship between outflow time scale and ejection rate.

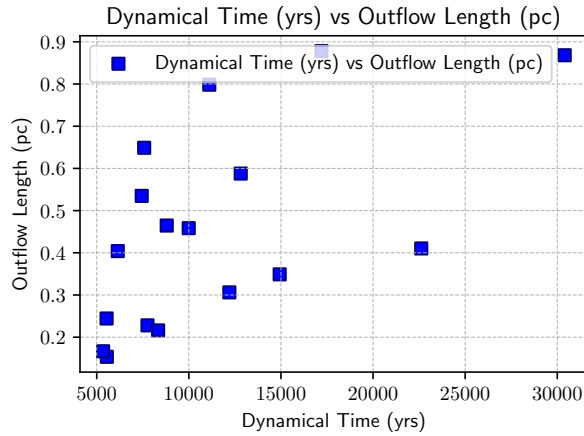


Figure 44: Outflow duration vs. physical length.

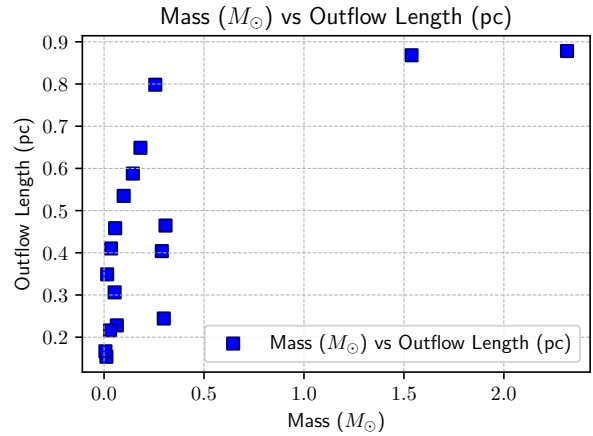


Figure 45: Mass vs. outflow length correlation.

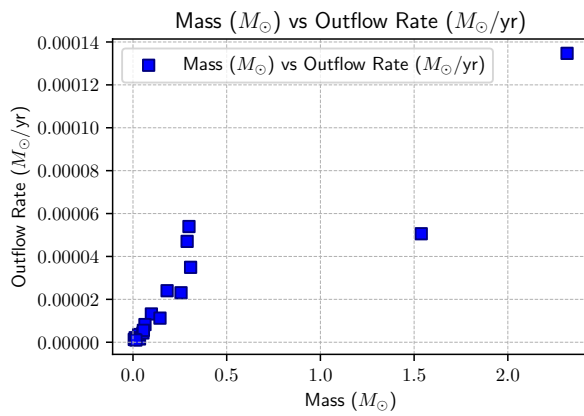


Figure 46: Relationship between outflow mass and ejection rate.

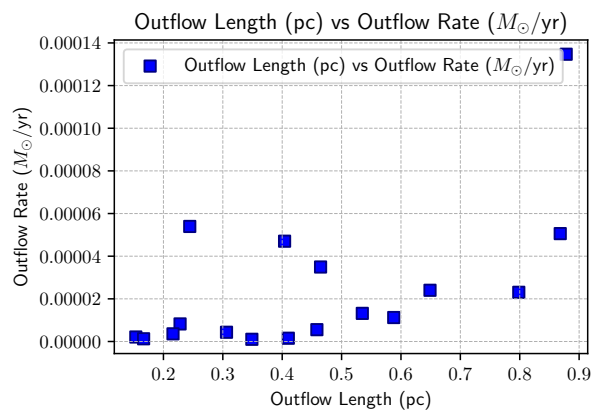


Figure 47: Correlation between outflow length and ejection rate.

## 8.3 Modelling Protostellar Outflows

### 8.3 PLUTO Code

PLUTO is an adaptable and modular computational code developed primarily for astrophysical research and the simulation of high Mach number flows in various spatial dimensions. It operates as a Godunov-type code, which refers to a class of numerical methods renowned for their ability to handle shock waves and discontinuities in fluid dynamics with high accuracy. Godunov-type methods are particularly effective in solving conservation laws by applying a finite volume approach and solving Riemann problems at cell interfaces [see 6, for more details].

PLUTO incorporates a range of hydrodynamic modules and algorithms, allowing it to tackle complex equations governing different types of fluids, including Newtonian fluids, relativistic fluids, and magnetohydrodynamic (MHD) or relativistic MHD fluids. These equations can be solved in both Cartesian and curvilinear coordinate systems, providing flexibility for various astrophysical scenarios.

Written entirely in the C programming language, PLUTO is designed for efficient performance across different computing environments. It supports execution on both single-processor systems and extensive parallel clusters, utilizing the MPI (Message Passing Interface) library to manage parallel computations effectively. This capability makes PLUTO well-suited for handling large-scale simulations.

Additionally, PLUTO offers a user-friendly interface based on Python scripting, which simplifies the process of setting up and configuring simulations. This interface facilitates ease of use, allowing researchers to define and customize their physical models without delving deeply into the code's technical details.

### Axisymmetric Jet Propagation

Protostellar jets are collimated, non-relativistic high-velocity outflows frequently observed in plasma environments. These jets, characterized by their interaction with magnetized plasma and the surrounding medium, are best modeled as magnetohydrodynamic (MHD) phenomena. The propulsion of these jets results from a combination of magnetic and thermal forces. As magnetic fields dynamically interact with ionized gases, they guide and focus the flow of charged particles into beam-like structures. The interplay between the magnetized plasma and the external medium leads to the formation of shocks and instabilities.

The axisymmetric jet problem is an important study in astrophysical fluid dynamics, typically addressing the propagation and behavior of jets in a cylindrical coordinate system. This problem involves several key physical principles and parameters, which are crucial for accurately modeling and understanding the behavior of these astrophysical jets. Here's an overview of the setup in PLUTO and underlying physics [6]:

## Physical Setup and Coordinates

The jet problem is analyzed in an axisymmetric cylindrical coordinate system  $(R, z)$ , where  $R$  is the radial coordinate and  $z$  is the axial coordinate. This setup simplifies the problem by assuming symmetry around the jet axis and is particularly useful for studying jets that exhibit cylindrical symmetry.

## Ambient and Jet Conditions

In this model, the ambient medium is considered at rest and characterized by a uniform density  $\rho_a$  and pressure  $p_a$ . The jet, emerging from a circular nozzle at the lower boundary of the domain, carries a constant poloidal magnetic field component  $B_z$  and a radially varying toroidal magnetic field component  $B_\phi(R)$ . The jet's flow variables are defined as:

- Density Contrast\*\*  $\eta = \rho_j/\rho_a$ , where  $\rho_j$  is the density within the jet and  $\rho_a$  is the density of the ambient medium. It affects the jet's buoyancy, stability, and interaction with the surrounding environment.
- Axial Velocity:  $v_z(R) = v_j$ , where  $v_j$  is the constant jet velocity. It affects how much the jet can penetrate into the external medium
- Toroidal Magnetic Field:  $B_\phi(R)$  varies with radius  $R$ :

$$B_\phi(R) = \begin{cases} -\frac{B_m R}{a} & \text{for } R < a \\ -\frac{B_m a}{R} & \text{for } R > a \end{cases}$$

where  $a$  is the magnetization radius and  $B_m$  is a constant. This parameter characterizes the magnetic field strength in the azimuthal direction.

- Poloidal Magnetic Field:  $B_z(R) = B_{z0}$ , a constant. This value indicates the strength of the magnetic field along the direction of the jet's propagation.

## Radial Pressure Balance

The radial pressure distribution is derived from the radial momentum balance equation, which considers thermal, centrifugal, and magnetic forces:

$$\frac{dp}{dR} = \frac{\rho v_\phi^2}{R} - \frac{1}{2} \left[ \frac{1}{R^2} \frac{d(R^2 B_\phi^2)}{dR} + \frac{dB_z^2}{dR} \right]$$

Assuming constant  $B_z$  and neglecting rotation simplifies the equation, yielding:

$$p(R) = p_a + B_m^2 \left[ 1 - \min \left( \frac{R^2}{a^2}, 1 \right) \right]$$

At the jet's axis ( $R = 0$ ), the pressure increases with the toroidal field:

$$p(R = 0) \equiv p_j = p_a + B_m^2$$

## Normalization and Parameters

To reduce the number of parameters, the following normalization choices are made:

- Length: Jet radius  $R_j = 1$ .
- Density: Ambient density  $\rho_a = 1$ .
- Velocity:
  - In the adiabatic case (no cooling), the ambient sound speed is set to  $c_a = \Gamma p_a / \rho_a = 1$ , leading to  $p_a = 1/\Gamma$ .
  - In the radiative case (with cooling), the velocity is set to 1 km/s, and the ambient pressure is derived from the ambient temperature  $T_a = 2500$  K.

## Magnetization and Average Magnetic Field

The average value of  $B_\phi^2$  is:

$$\langle B_\phi^2 \rangle = B_m^2 a^2 \left( \frac{1}{2} - 2 \log a \right)$$

The magnetization parameters are used to relate the magnetic field strengths to the pressure:

$$B_z^2 = 2\sigma_z p_a$$

$$B_m^2 = \frac{2\sigma_\phi}{a^2 \left( \frac{1}{2} - 2 \log a \right)} p_a$$

## Setup

The PLUTO code has been employed to simulate jets, which serve as precursors to outflows. Given the complexities involved in recreating observational outflows, particularly due to the lack of detailed information regarding the molecular cloud and associated chemistry, this study has focused on investigating the effects of varying parameters within the PLUTO framework. The objective was to discern how alterations in these parameters influence the simulation outcomes. Through systematic exploration and analysis, conclusions were drawn regarding which parameters should be enabled or adjusted in the setup to enhance the effectiveness of the simulations.

Following the installation of PLUTO, a directory named PLUTO, containing several subdirectories including 'Test Problems', was created. The environment variable PLUTO\_DIR was set to point to the code directory, and this setting was included in the `.bashrc` file. The working directory was then changed to `Test Problems > MHD > Jet`.

Default header and initialization files were present in the directory. Working files were created by copying the desired default files:

```
cp definitions_06.h definitions.h
cp pluto_06.ini pluto.ini
```

The Python script `setup.py` was executed with the command:

```
python $PLUTO_DIR/setup.py
```

This script initiated a menu where the 'Setup Problem' option was selected to configure a 2D problem with default parameters. Upon proceeding, the MHD Menu appeared, allowing the setup of the physics of the problem, including the equation of state and various forces acting on the system. A subsequent menu allowed the specification of user-defined parameters. The `Linux.gcc.defs` option was selected in the change makefile menu.

Initial conditions were specified in the `pluto.ini` file. Parameters were edited using:

```
nano pluto.ini
```

Different parameters were set for various iterations. To obtain multiple instances of the problem, the `db1` parameter was adjusted to 1.0 to define the output file interval. The configuration was changed from 'single file' to 'multiple files'. The total simulation time was set to 10, allowing for visualization of the simulation over 10 frames. A Python script was developed to extract output variables from the `.dbl` files and generate plots. Additionally, animations were created from the sequential frame images.

### 8.3 Results with different parameter setup

#### Default Configuration Parameters

```
PHYSICS: MHD
DIMENSIONS: 2
GEOMETRY: CYLINDRICAL
BODY_FORCE: NO
COOLING: NO
RECONSTRUCTION: LINEAR
TIME_STEPPING: RK2
NTRACER: 1
PARTICLES: NO
USER_DEF_PARAMETERS: 4

EOS: PVTE_LAW
DIVB_CONTROL: CONSTRAINED_TRANSPORT
VISCOSITY: NO
```

```

[Grid]
X1-grid    1    0.0    160    u    10.0
X2-grid    1    0.0    480    u    30.0
X3-grid    1    0.0      1    u    1.0

[Time]
CFL          0.4
CFL_max_var 1.1
tstop        0.6
first_dt    1.e-6

[Solver]
Solver       hlld

[Boundary]
X1-beg      axisymmetric
X1-end      outflow
X2-beg      userdef
X2-end      outflow
X3-beg      outflow
X3-end      outflow

[Static Grid Output]
uservar     1      tmp
dbl         0.06  -1   multiple_files
flt         1.0   -1   single_file  cgs
vtk         -1.0  -1   single_file
log         10
analysis   -1.0  -1

[User defined Parameters]
ETA          0.1
JET_VEL     150.0
SIGMA_Z     0.5
SIGMA_PHI   0.5

```

These are some of the major default parameters. Any changes to these parameters are noted explicitly. In the remaining simulations, only parameters that differ from the default values are mentioned in the headings.

## Default

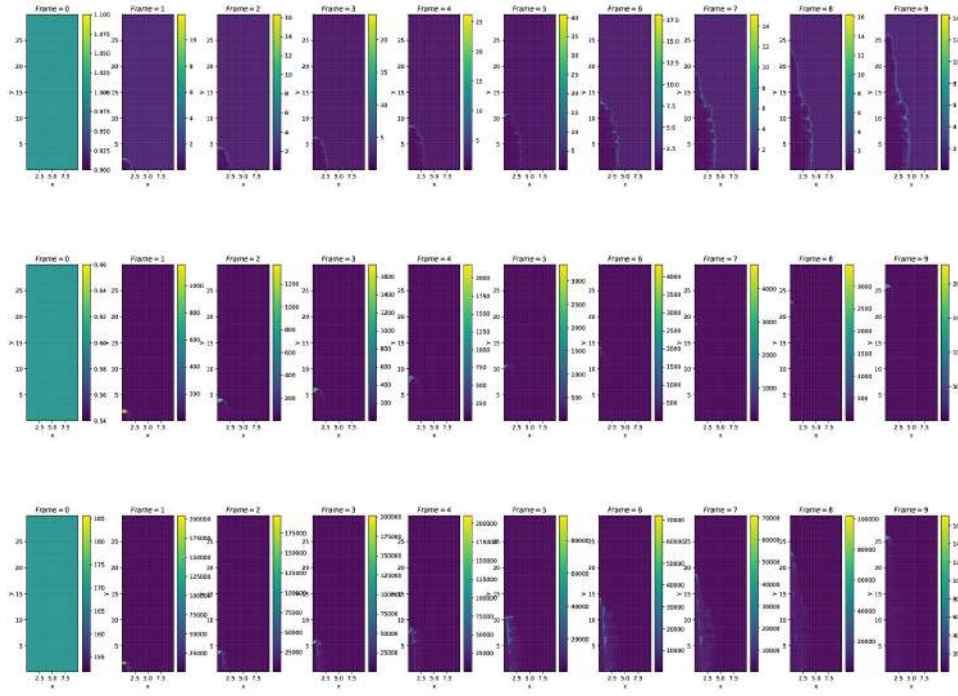


Figure 48: Time-evolution of density, pressure, and temperature respectively for default values

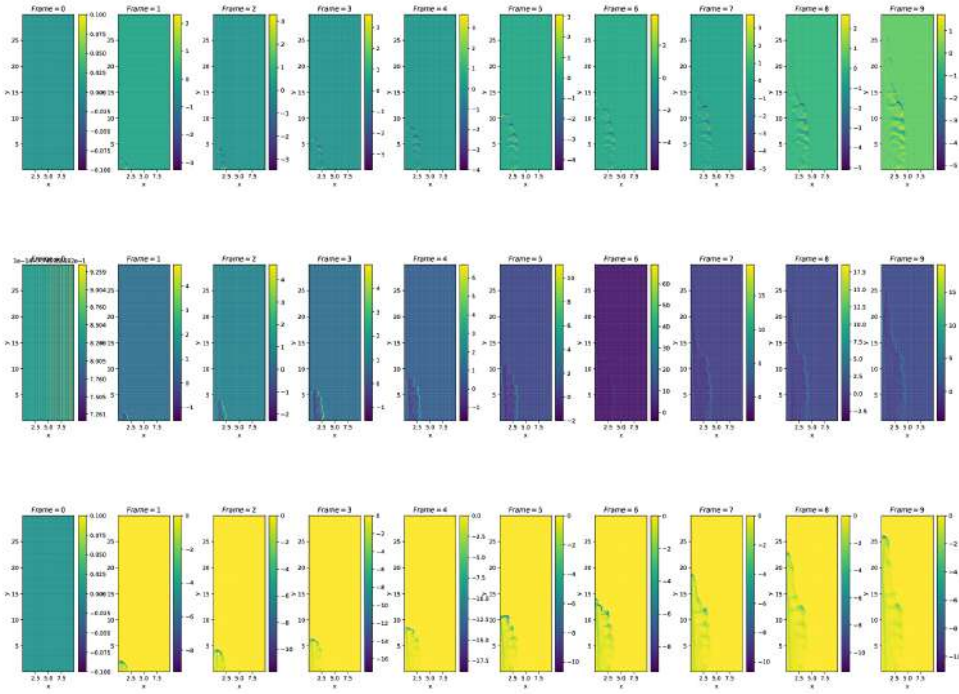


Figure 49: Time-evolution of the radial, azimuthal, and z component of the magnetic field respectively

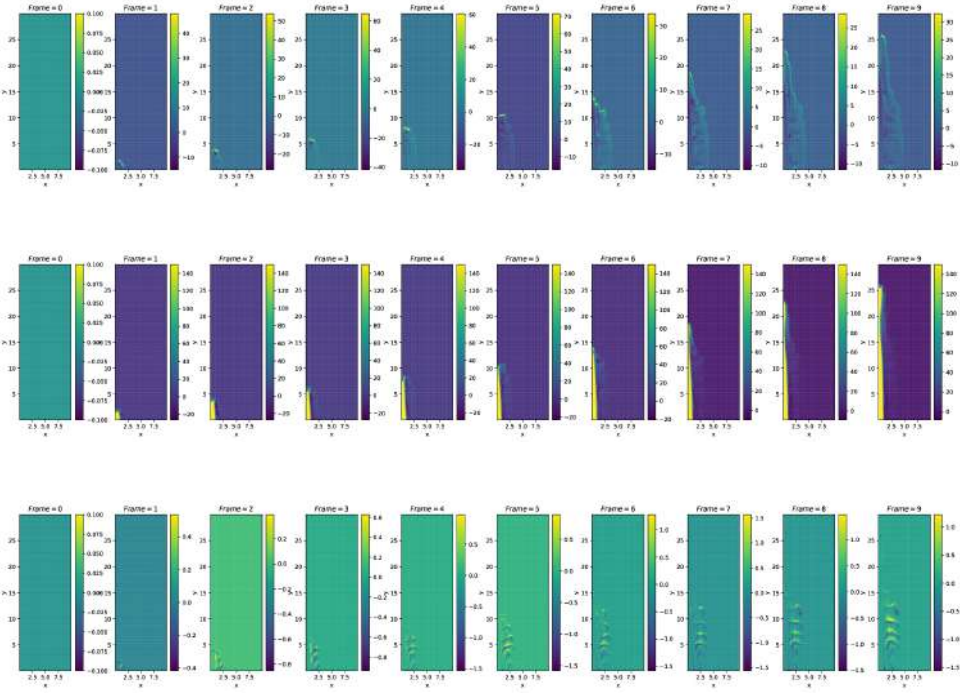


Figure 50: Time-evolution of the radial, azimuthal, and z component of velocity respectively for default values

$\eta = 0.05$

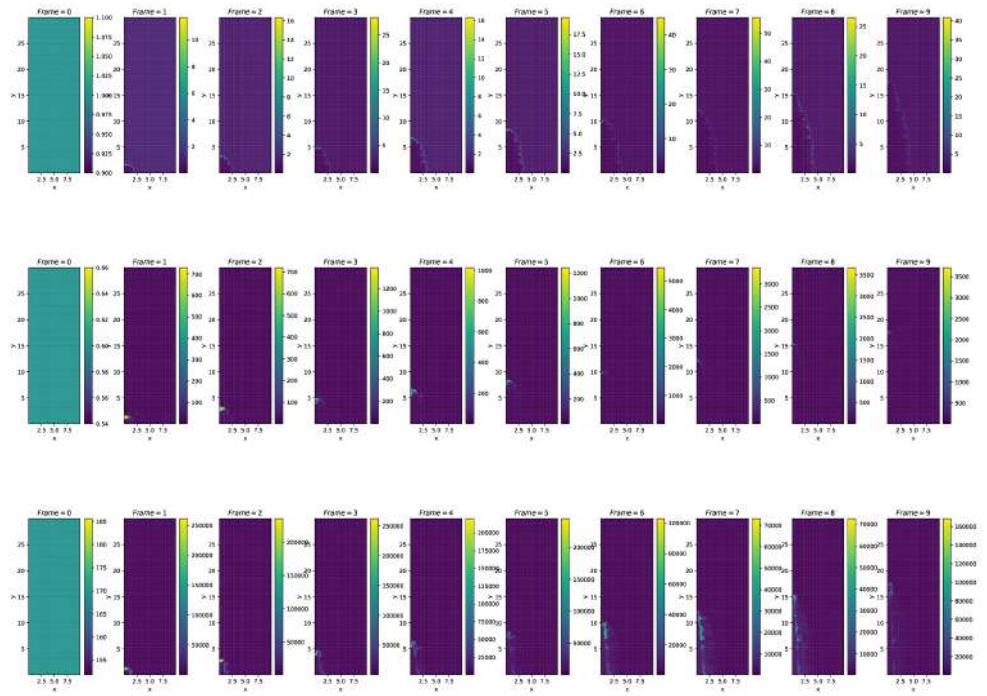


Figure 51: Time-evolution of density, pressure, and temperature respectively for  $\eta = 0.05$

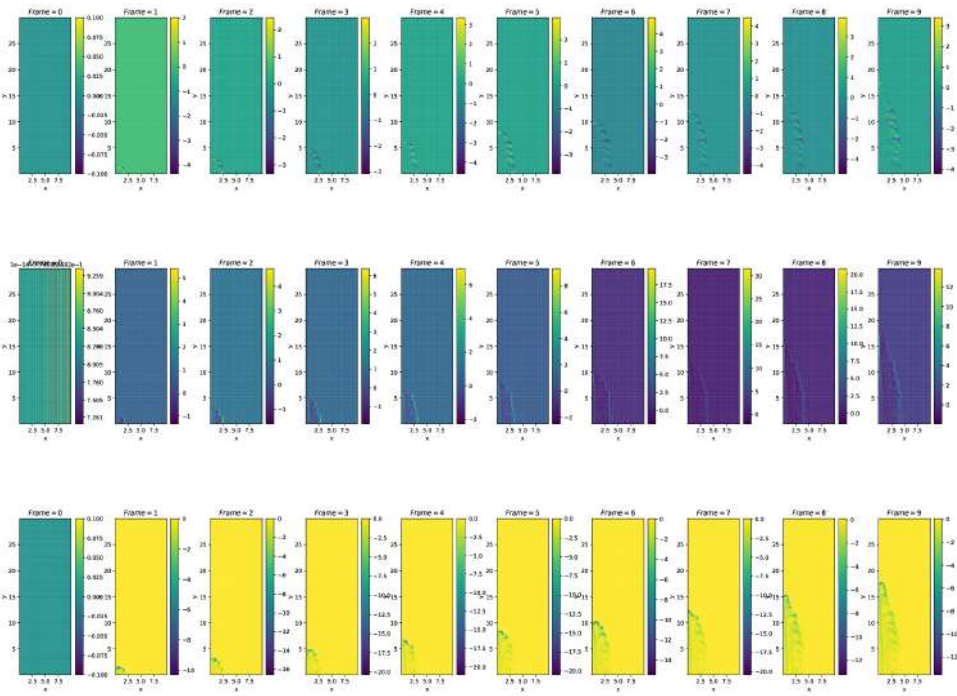


Figure 52: Time-evolution of the radial, azimuthal, and z component of the magnetic field respectively for  $\eta = 0.05$

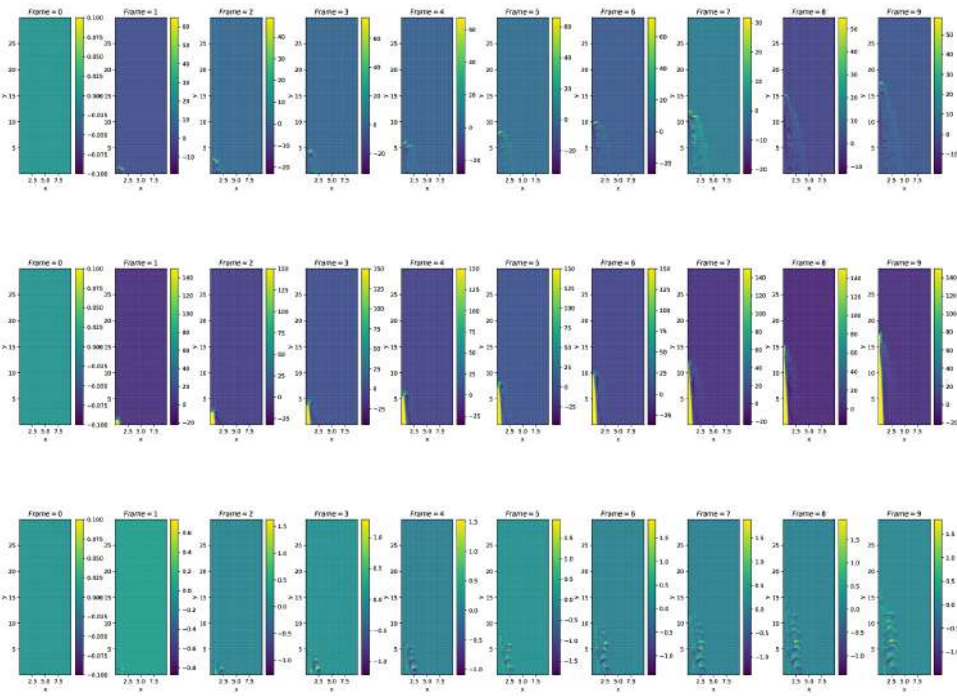


Figure 53: Time-evolution of the radial, azimuthal, and z component of velocity respectively for  $\eta = 0.05$

## Ideal equation of state

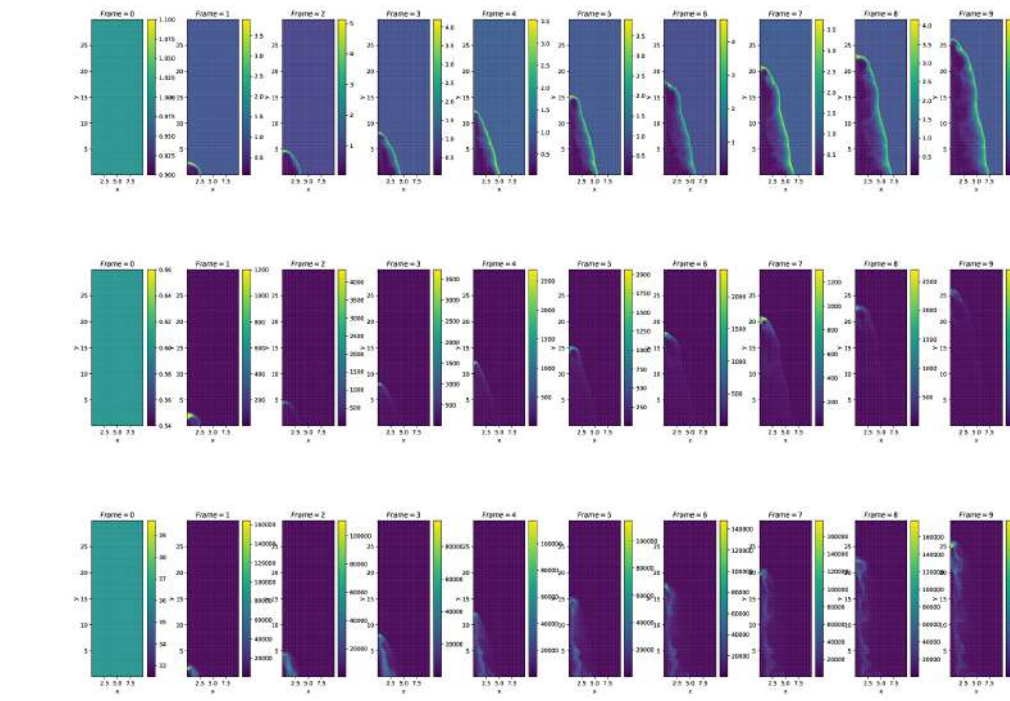


Figure 54: Time-evolution of density, pressure, and temp. respectively Ideal EoS

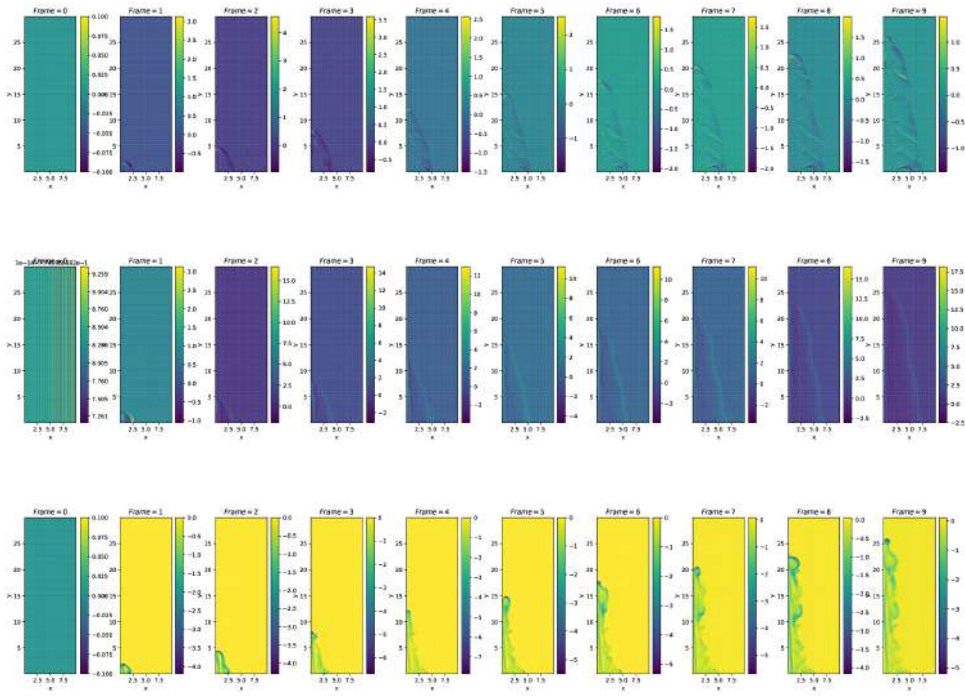


Figure 55: Time-evolution of the radial, azimuthal, and z components of the mag. field respectively

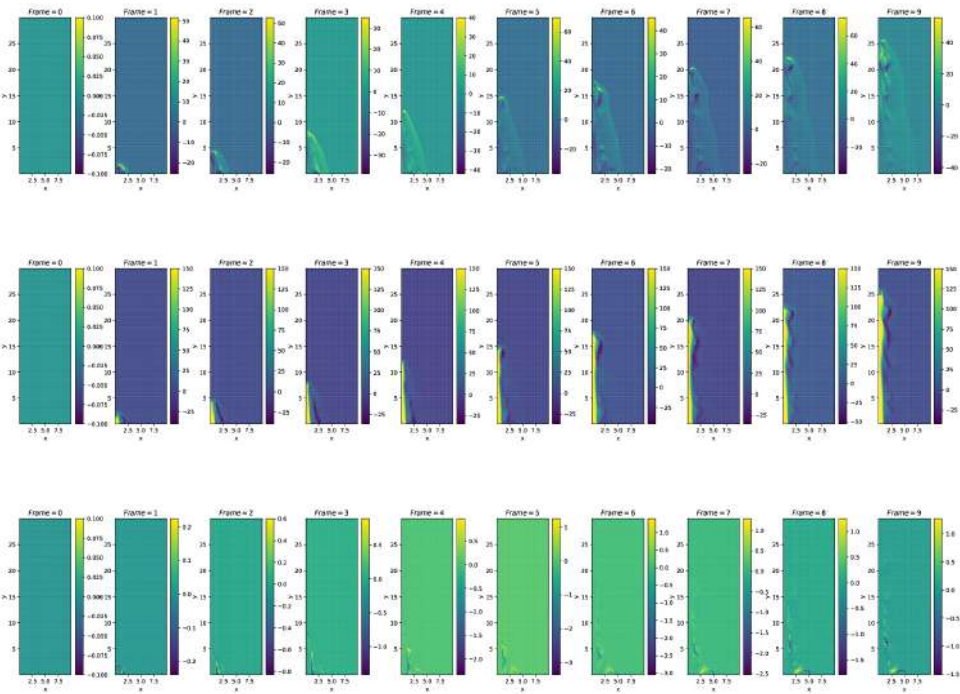


Figure 56: Time-evolution of the radial, azimuthal, and z component of velocity respectively for Ideal EoS

**Ideal equation of state, Body force vector,  $\eta = 0.1$  and jet velocity = 100 km/s**

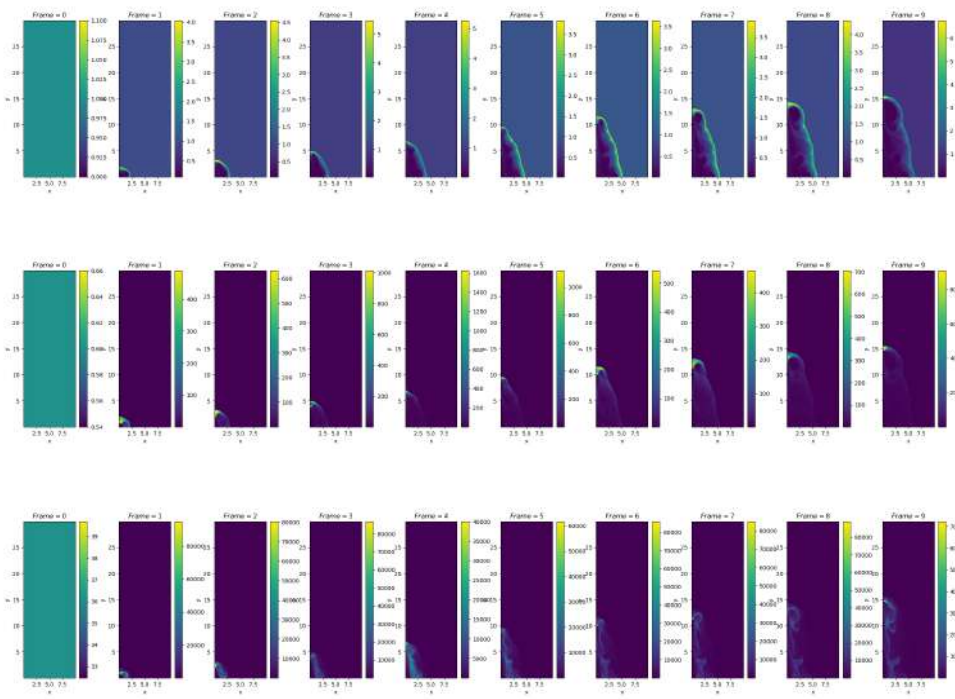


Figure 57: Time-evolution of density, pressure and temp. respectively for  $\eta = 0.1$  and jet vel. = 100 km/s

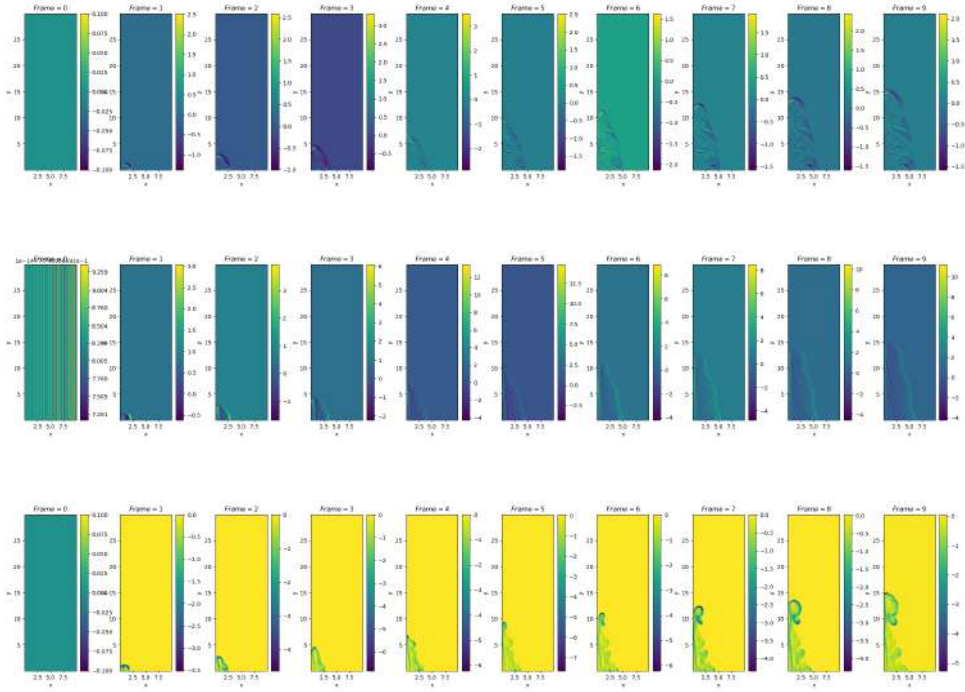


Figure 58: Time-evolution of the radial, azimuthal and z component of mag. field respectively for  $\eta = 0.1$  & jet vel. = 100 km/s

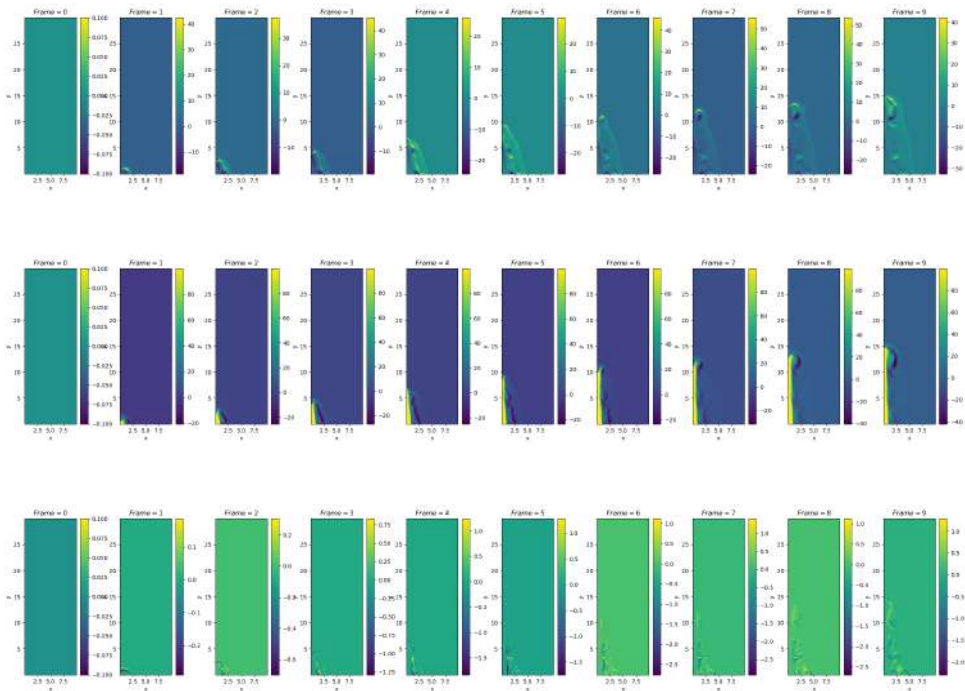
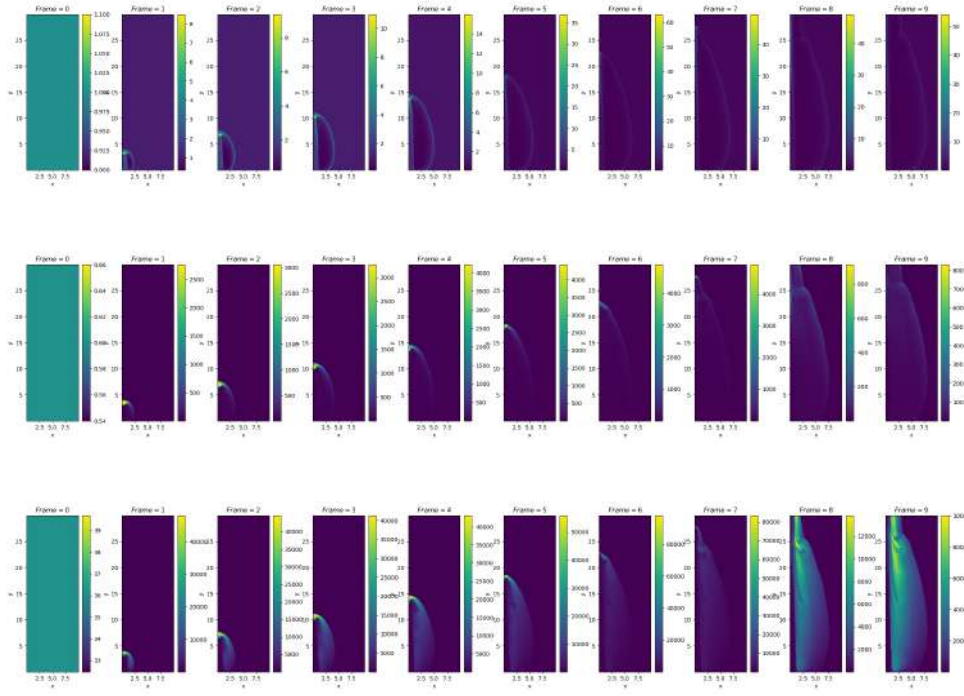
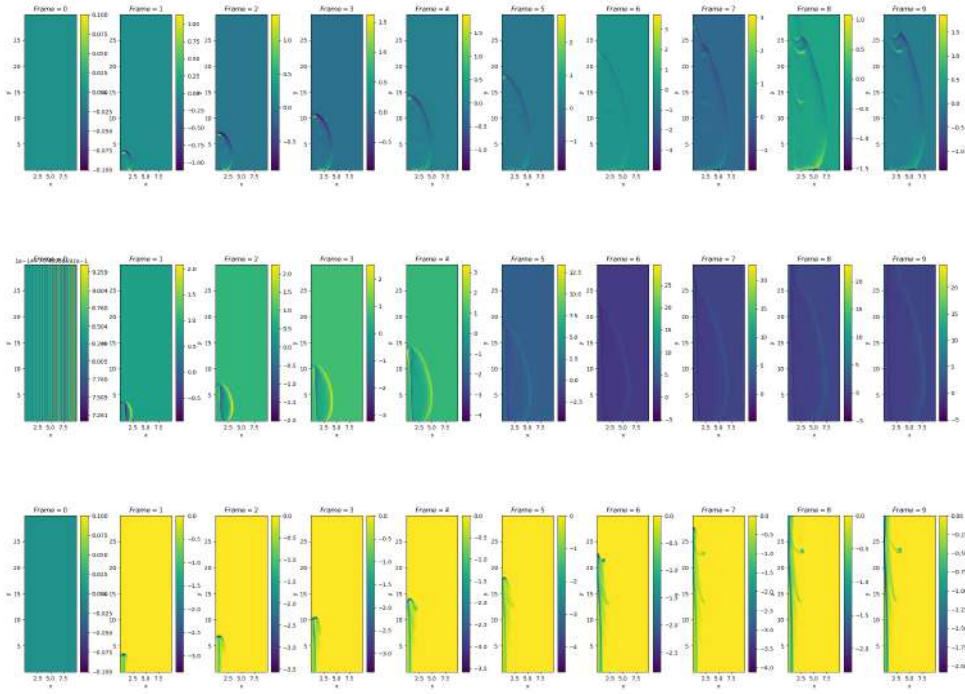


Figure 59: Time-evolution of the radial, azimuthal and z component of vel. respectively for  $\eta = 0.1$  and jet vel. = 100 km/s

Ideal equation of state, Body force vector,  $\eta = 2$  and jet velocity = 100 km/sFigure 60: Time-evolution of density, pressure and temp. respectively for  $\eta = 2$  and jet vel. = 100 km/sFigure 61: Time-evolution of the mag. field components respectively for  $\eta = 2$  and jet vel. = 100 km/s

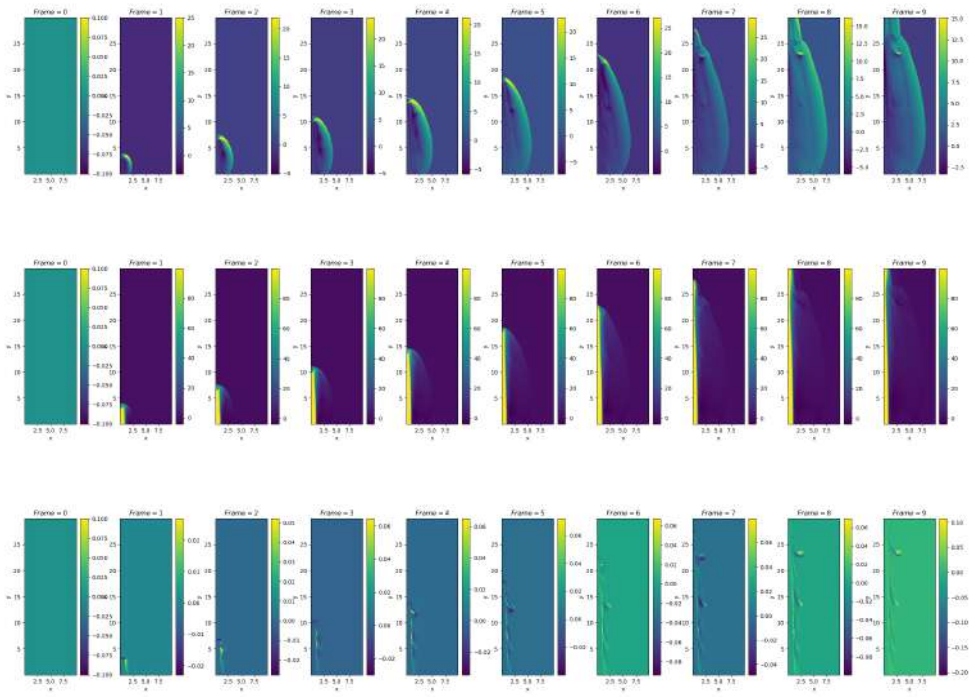


Figure 62: Time-evolution of the radial, azimuthal and z component of vel. respectively for  $\eta = 2$  and jet vel. = 100 km/s

### Ideal equation of state, Body force vector, $\eta = 10$ and jet velocity = 100 km/s

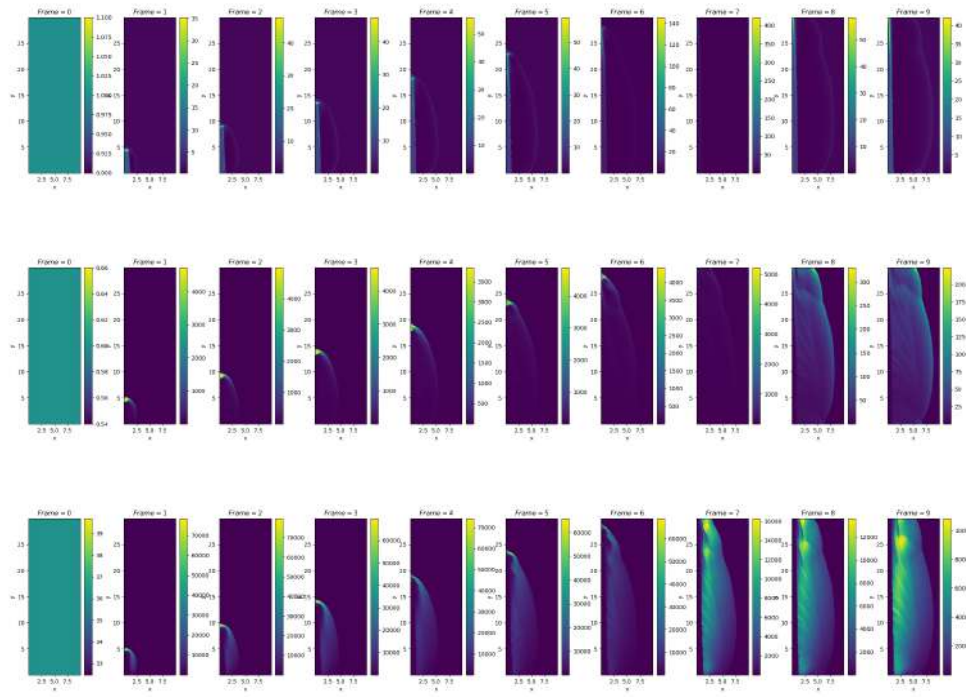


Figure 63: Time-evolution of density, pressure and temp. respectively for  $\eta = 10$  and jet vel. = 100 km/s

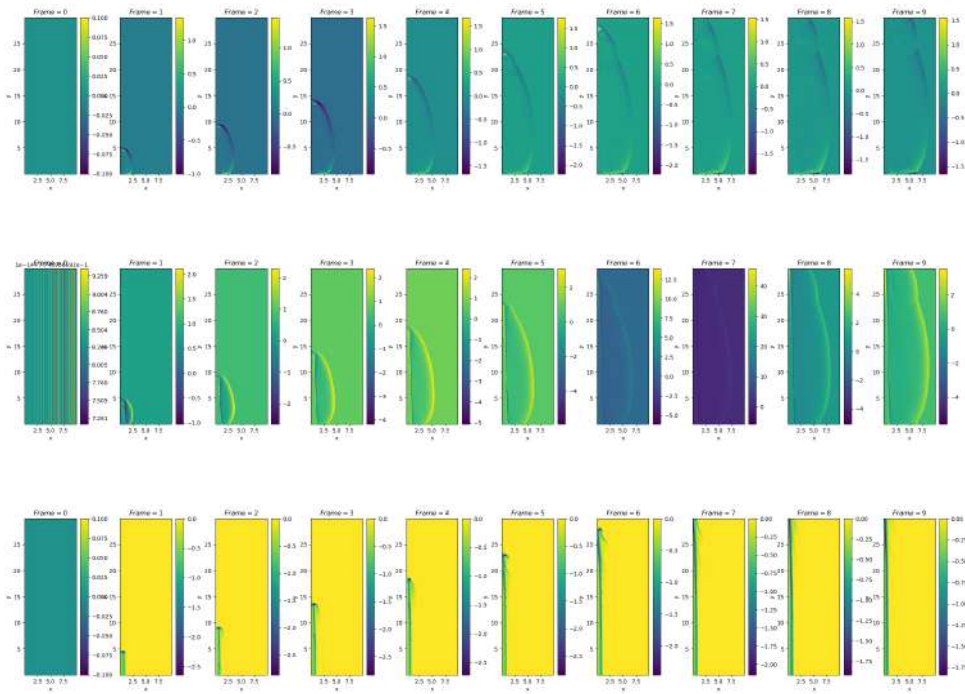


Figure 64: Time-evolution of the radial, azimuthal and z component of magnetic field respectively for  $\eta = 10$  and jet velocity = 100 km/s

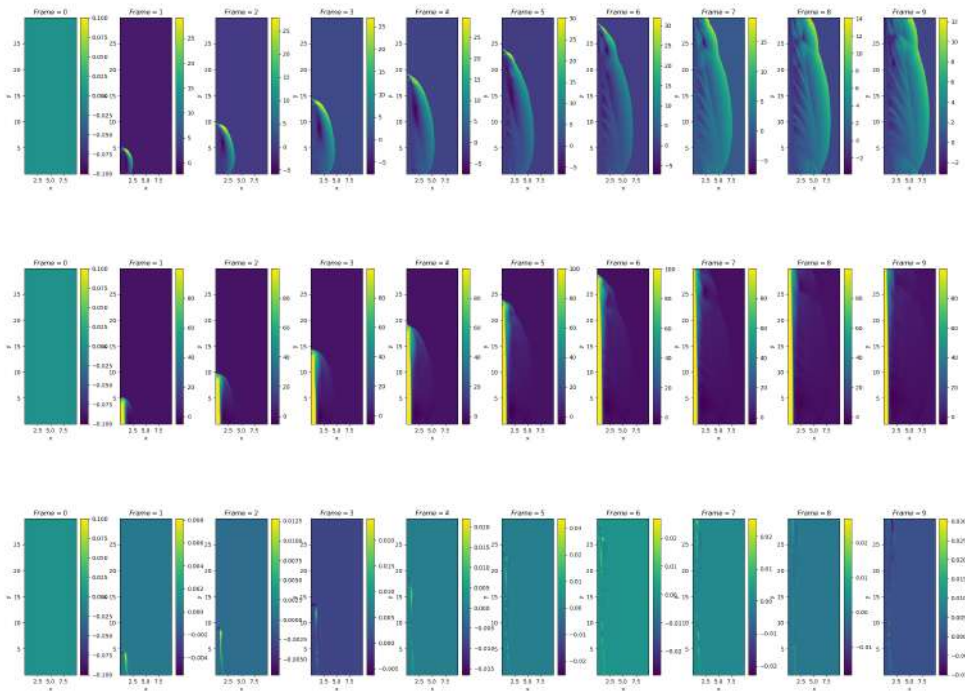


Figure 65: Time-evolution of the radial, azimuthal and z component of velocity respectively for  $\eta = 10$  and jet velocity = 100 km/s

**Body Force Vector + Potential,  $\eta = 10$  and jet velocity = 100 km/s**

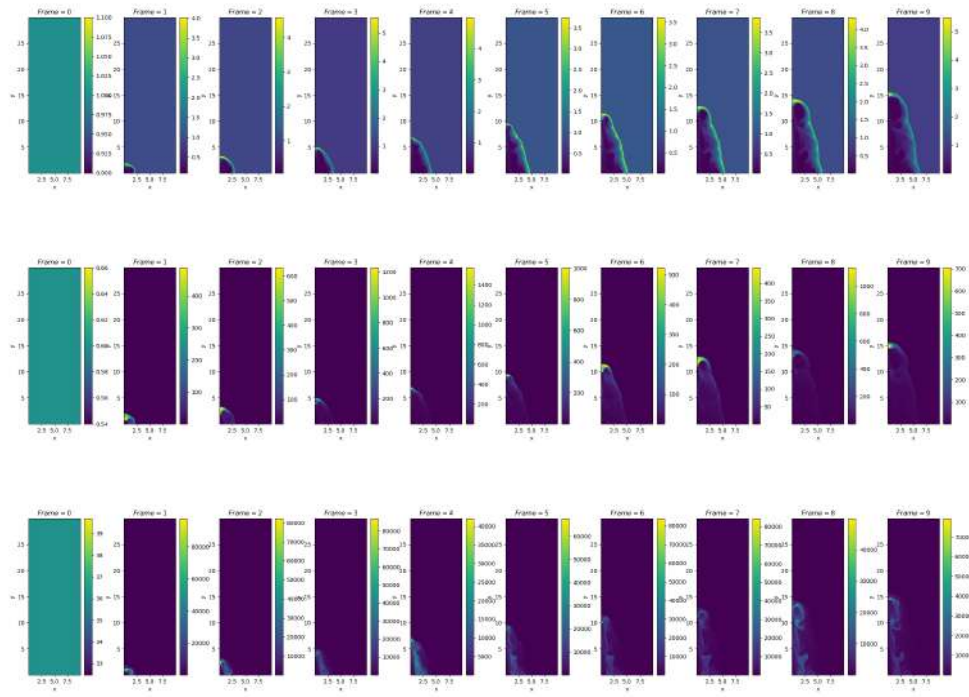


Figure 66: Time-evolution of density, pressure, and temperature respectively with body forces

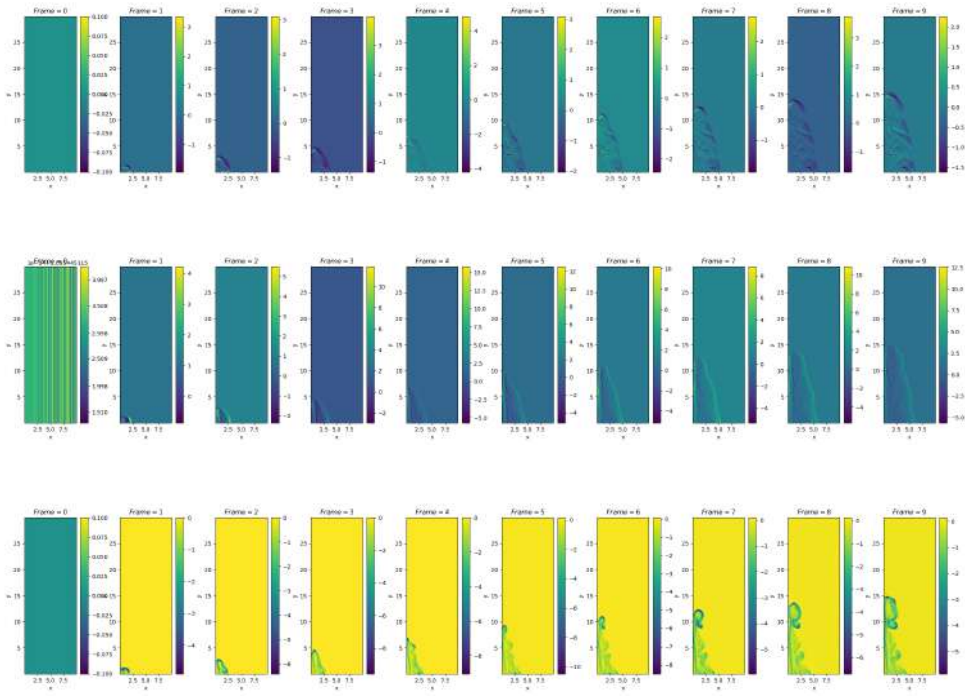


Figure 67: Time-evolution of the mag. field components with body forces

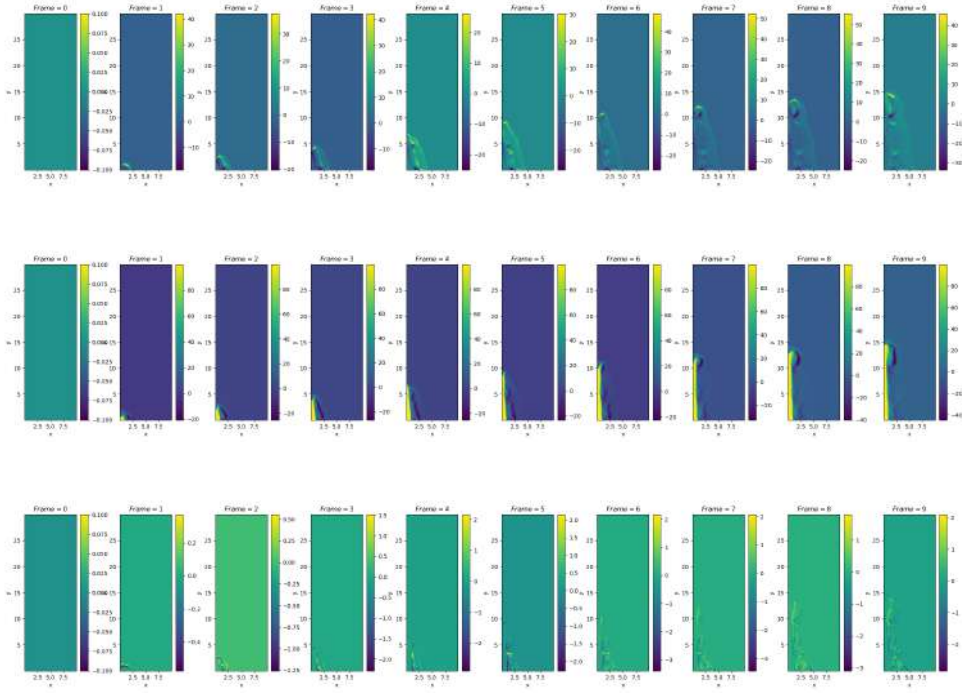


Figure 68: Time-evolution of the radial, azimuthal, and z component of velocity respectively with body forces

## 9 Conclusion & Suggestion of Research Project

### Simulation

The collimated jet-like structure and its subsequent broadening due to interaction with the interstellar medium are clearly visible. This phenomenon is also evident in the density and velocity profiles, where the presence of knot-like structures—also observed in observational data—can be discerned, as illustrated by the position-velocity diagrams. The magnetic field is typically observed to be weaker at the central column and stronger at the interface between the jet and the external medium. In scenarios where the ideal equation of state is applied, finger-like structures appear along the interface, possibly indicating Rayleigh-Taylor instabilities. The jet's greater acceleration perpendicular to the z-axis corresponds to a larger effective gravity, which sets the stage for these instabilities. These effects become more pronounced when body forces are introduced into the simulation, leading to an increase in effective gravity. Pressure profiles reveal that pressure is lower in the main column and increases laterally outward. Additionally, pressure rises more rapidly in the direction of propagation than laterally, with the jet's tip exhibiting an extremely high pressure compared to the central region at the jet's origin.

In all simulations, constrained transport is employed to enforce the zero divergence condition of the magnetic field. The value of  $\eta$  appears to have a significant influence on the extent of the jet, with body forces also playing a crucial role. The final simulation, which includes both vector and

gravitational body forces, provides a more accurate representation of the real situation.

## 10 Future Scope

### Data Analysis

In the future, the same regions may be studied using alternative tracers to determine whether this approach leads to improved identification of outflows. Additionally, a similar analytical methodology will be applied to other regions to assess the consistency and reliability of the findings across different environments.

By employing various tracers, researchers aim to enhance the sensitivity and specificity of outflow detection, thereby enriching the understanding of the underlying physical processes. The replication of this analysis in diverse regions will facilitate comparisons and potentially reveal broader patterns in outflow characteristics, contributing to a more comprehensive understanding of star formation processes.

### Simulation

The study of protostellar outflows is incomplete without addressing the chemical processes involved. When the jet interacts with the external medium, various chemical reactions produce key tracers such as CO, HCO<sup>+</sup>, and SiO. The number densities of these species are not fixed, yet all previous simulations have assumed constant number densities. Future simulations should incorporate chemical processes to achieve results that more closely align with observations. This is feasible in PLUTO with the integration of additional software, though the process is complex and warrants further exploration.

Additional necessary modifications include the incorporation of dust in the simulations, which was not possible due to the unavailability of the required module. Another important consideration is the inclusion of appropriate cooling mechanisms, which are closely linked to the chemistry and should not be selected ad hoc. A better understanding of the chemistry will also enable the use of a custom equation of state tailored to the specific physical conditions.

## 11 Results Achieved

1. Identification of outflows in Molecular clouds
2. Calculation of dynamical properties of the outflows
3. Basic simulations of outflows with different parameters

All the Python Code written for the analysis is provided here

## 12 References

- [1] J. Bally, “Protostellar outflows”, *Annual Review of Astronomy and Astrophysics*, vol. 54, pp. 491–528, 2016. DOI: [10.1146/annurev-astro-081915-023341](https://doi.org/10.1146/annurev-astro-081915-023341).
- [2] L. Hartmann, *Accretion Processes in Star Formation* (Cambridge Astrophysics), 2nd ed. Cambridge University Press, 2008.
- [3] T. Baug, K. Wang, T. Liu, *et al.*, “Alma observations reveal no preferred outflow-filament and outflow-magnetic field orientations in protoclusters”, *The Astrophysical Journal*, vol. 890, no. 1, p. 44, Feb. 2020. DOI: [10.3847/1538-4357/ab66b6](https://doi.org/10.3847/1538-4357/ab66b6). [Online]. Available: <https://doi.org/10.3847/1538-4357/ab66b6>.
- [4] H. G. Arce, D. Shepherd, F. Gueth, *et al.*, *Molecular outflows in low- and high-mass star forming regions*, American Museum of Natural History; National Radio Astronomy Observatory; Institut de Radioastronomie Millimétrique, Grenoble; Harvard-Smithsonian Center for Astrophysics; Observatorio Astronómico Nacional; Max-Planck-Institut für Radioastronomie; Max-Planck-Institut für Astronomie, Mar. 2006. arXiv: [astro-ph/0603071v1](https://arxiv.org/abs/astro-ph/0603071).
- [5] T. Baug, K. Wang, T. Liu, *et al.*, “An alma study of outflow parameters of protoclusters: Outflow feedback to maintain the turbulence”, *Monthly Notices of the Royal Astronomical Society*, vol. 507, pp. 4316–4334, Jul. 2021, Advance Access publication 2021 July 6. Accepted 2021 June 30. Received 2021 June 30; in original form 2020 September 24. DOI: [10.1093/mnras/stab1902](https://doi.org/10.1093/mnras/stab1902).
- [6] A. Mignone, G. Bodo, S. Massaglia, *et al.*, “Pluto: A numerical code for computational astrophysics”, *The Astrophysical Journal Supplement Series*, vol. 170, pp. 228–242, May 2007, All rights reserved. Printed in U.S.A. DOI: [10.1086/513316](https://doi.org/10.1086/513316). [Online]. Available: <https://iopscience.iop.org/article/10.1086/513316>.
- [7] U. Lebreuilly, P. Hennebelle, A. Maury, *et al.*, “Influence of protostellar outflows on star and protoplanetary disk formation in a massive star-forming clump”, *Astronomy & Astrophysics*, vol. 683, A13, 2024, Published online 28 February 2024. DOI: [10.1051/0004-6361/202347913](https://doi.org/10.1051/0004-6361/202347913). [Online]. Available: <https://doi.org/10.1051/0004-6361/202347913>.
- [8] A. Frank, T. Ray, S. Cabrit, *et al.*, “Jets and outflows from star to cloud: Observations confront theory”, *arXiv:1402.3553v1 [astro-ph.SR]*, Feb. 2014, 14 Feb 2014.
- [9] S. Sheiknezami, C. Fendt, O. Porth, B. Vaidya, and J. Ghanbari, “Bipolar jets launched from magnetically diffusive accretion disks. i. ejection efficiency versus field strength and diffusivity”, *The Astrophysical Journal*, vol. 757, no. 1, p. 65, Sep. 2012, All rights reserved. Printed in the U.S.A. DOI: [10.1088/0004-637X/757/1/65](https://doi.org/10.1088/0004-637X/757/1/65). [Online]. Available: <https://iopscience.iop.org/article/10.1088/0004-637X/757/1/65>.

- [10] R. E. Pudritz and T. P. Ray, “The role of magnetic fields in protostellar outflows and star formation”, *Frontiers in Astronomy and Space Sciences*, vol. 6, p. 54, 2019. DOI: 10.3389/fspas.2019.00054.
- [11] U. Lebreuilly, P. Hennebelle, A. Maury, *et al.*, “Influence of protostellar outflows on star and protoplanetary disk formation in a massive star-forming clump”, *arXiv:2309.05397*, 2023.
- [12] P. F. Rohde, S. Walch, D. Seifried, A. P. Whitworth, and S. D. Clarke, “Protostellar outflows: A window to the past”, *Monthly Notices of the Royal Astronomical Society*, vol. 510, no. 2, pp. 2552–2571, 2022. DOI: 10.1093/mnras/stab3572.
- [13] A. Frank, T. P. Ray, S. Cabrit, *et al.*, “Jets and outflows from star to cloud: Observations confront theory”, *arXiv:1402.3553v1 [astro-ph.SR]*, Feb. 2014, 14 Feb 2014.
- [14] Spectral Cube, *Moments in spectral cube*, Accessed: 2024-10-12, 2023. [Online]. Available: <https://spectral-cube.readthedocs.io/en/latest/moments.html>.

## 13 Declaration

I Sanjana Gupta hereby declare that the details/facts mentioned above are true to the best of my knowledge and I solely be held responsible in case of any discrepancies found in the details mentioned above.



(Signature of Scholar)

Date: 18.10.2024

Place: Kolkata